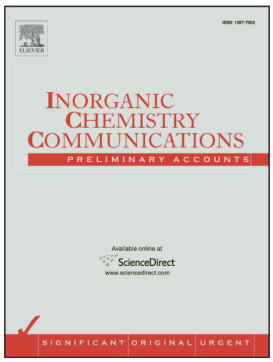

Core-shell zinc phosphate/biopolymer nanocomposites: comparative anticorrosion and antibacterial performance of cellulose and chitosan coatings on mild steel

Faezeh Mohammadkhani, Arezoo Mohammadkhani, Nazanin Farhadyar, Payam Hayati, Constantinos D. Zeinalipour-Yazdi, Saeed Khodabakhshi

PII: S1387-7003(26)01030-0

DOI: https://doi.org/10.1016/j.inoche.2026.117163

Reference: INOCHE 117163

To appear in: *Inorganic Chemistry Communications*

Received date: 31 March 2026

Revised date: 30 June 2026

Accepted date: 3 July 2026

Please cite this article as: F. Mohammadkhani, A. Mohammadkhani, N. Farhadyar, et al., Core-shell zinc phosphate/biopolymer nanocomposites: comparative anticorrosion and antibacterial performance of cellulose and chitosan coatings on mild steel, *Inorganic Chemistry Communications* (2026), https://doi.org/10.1016/j.inoche.2026.117163

Core-Shell Zinc Phosphate/Biopolymer Nanocomposites: Comparative Anticorrosion and Antibacterial Performance of Cellulose and Chitosan Coatings on Mild Steel

Faezeh Mohammadkhani[a], Arezoo Mohammadkhani [b]*, Nazanin Farhadyar[c]**, Payam Hayati [d]***, Constantinos D. Zeinalipour-Yazdi[e], Saeed Khodabakhshi[f],

[a] *Department of Environmental Engineering, Faculty of Engineering, North Tehran Branch, Islamic Azad University, Tehran, Iran.*

[b] *Department of Chemistry, Fir. C., Islamic Azad University, Firoozabad, Iran*

[c]*Department of Chemistry, Varamin Pishva Branch, Islamic Azad University, Varamin, Iran*

[d]*Department of Biotechnology and Life Sciences, University of Insubria, Via Jean Henry Dunant, 3, 21100 Varese, Italy*

[e]*Faculty of Computing, Mathematics, Engineering and Natural Sciences, Northeastern University London, 1 Portsoken Street, E1 8BT, London, UK*

[f]*Energy Safety Research Institute, Swansea University, Bay Campus, Swansea, SA1 8EN, UK*

Corresponding Authors: *Email: arezoomohammadkhanichemist@yahoo.com; **Email: n.farhadyar98@gmail.com,*** Email: payam.hayati@uninsubria.it, payamhayati@yahoo.com

Abstract

The corrosion of mild steel in chloride-rich environments, exacerbated by microbial colonization and biofilm formation, remains a critical challenge for industrial infrastructure. A dual-functional zinc phosphate–biopolymer nanocomposite system was developed to enhance the corrosion resistance and antibacterial protection of mild steel in saline solution. Zinc-

phosphate nanoparticles (average diameter 36.25 nm) were stabilized using cellulose (ZnP@Cel, shell thickness 5.25 nm) and chitosan (ZnP@Ch, shell thickness 4 nm), forming uniform core–shell structures as confirmed by TEM and FTIR, where coordination interactions dominated in ZnP@Ch and hydrogen-bonding governed ZnP@Cel. Electrochemical measurements in 3.5 wt.% NaCl revealed a superior barrier performance for ZnP@Cel, achieving a corrosion inhibition efficiency of 75.3% under the tested conditions (3.5 wt.% NaCl, 24 h immersion) and reducing the corrosion current density from 7.12 to 1.76 $\mu A \cdot cm^{-2}$. EIS analysis further demonstrated the highest charge-transfer resistance (6127 $\Omega \cdot cm^2$) and elevated low-frequency impedance, indicating the formation of a compact and protective interfacial layer. In parallel, antibacterial assays against Streptococcus mutans confirmed significant bacterial reduction for both nanocomposites, with ZnP@Cel exhibiting complete inhibition while maintaining cytocompatibility. The integrated electrochemical and biological results highlight the potential of ZnP@Cel as an eco-friendly, dual-function protective material for steel structures exposed to corrosive and microbially active environments. The integrated electrochemical and biological results highlight the potential of ZnP@Cel as an eco-friendly, dual-function protective material for steel structures exposed to corrosive and microbially active environments.

Keywords*:* Zinc Phosphate-Chitosan; Zinc-Phosphate-Cellulose Nanocomposites; Corrosion Inhibition; Antibacterial Nanocomposites; Core-Shell Nanostructures.

1. Introduction

The corrosion of mild steel in chloride-rich environments such as 3.5 wt.% NaCl solution represents a major threat to industrial infrastructure durability [1,2]. Also the marine industry constantly develops new coatings to protect ships made from mild steel [1]. Chloride ions penetrate passive oxide layers and trigger localized pitting and crevice corrosion, accelerating metal dissolution and failure [3]. Microbiologically influenced corrosion (MIC) further

intensifies this process through biofilm formation and secretion of aggressive metabolites like sulfides and organic acids [4,5]. These synergistic mechanisms create a complex degradation environment that conventional inhibitors fail to control effectively, emphasizing the need for advanced, multifunctional protective systems [6,7]. Nanostructured materials, particularly zinc phosphate ($Zn_3(PO_4)_2$, ZP), have emerged as eco-friendly candidates capable of providing both corrosion inhibition and antibacterial protection through passive film formation and controlled ion release [8–15].

Moreover, ZP nanoparticles serve as reservoirs for the controlled release of Zn^{2+} and PO_4^{3-} ions, imparting self-healing characteristics and sustained protection in chloride-rich environments [2,3]. Beyond corrosion resistance, ZP also exhibits intrinsic antibacterial activity, primarily through zinc ion-mediated disruption of bacterial membranes and interference with metabolic pathways. When integrated into organic matrices, ZP can further synergize with polymers to improve antimicrobial efficacy, suppress biofilm formation, and extend the service life of metallic components [4,5]. Antibacterial nanocomposite coatings containing graphene derivatives and bioactive inorganic phases have recently shown strong potential for suppressing microbial growth while simultaneously improving corrosion resistance in aggressive environments[6]. Smart graphene-based nanocomposite coatings capable of combining corrosion resistance with adaptive and multifunctional surface behavior have recently attracted significant attention for advanced industrial applications[7]. Similar improvements in electrochemical barrier resistance and charge-transfer impedance have been observed in reduced graphene oxide/nitride reinforced epoxy coatings developed for marine steel applications[8]. Recent studies have demonstrated that hybrid inorganic-carbon nanofillers such as mixed metal nitride/graphene oxide systems significantly enhance barrier resistance, coating compactness, and mechanical durability through synergistic interfacial interactions within polymeric matrices[9]. Multifunctional nanocomposite coatings

incorporating graphitic carbon nitride and silanized ceramic nanofillers have also been reported to simultaneously improve corrosion resistance, thermal stability, and interfacial adhesion in harsh marine environments[10]. Recent reviews on graphene-based nanocomposite systems have highlighted the importance of nanoscale interfacial engineering, tortuous diffusion pathways, and hybrid filler architectures in improving long-term corrosion protection performance[11]. Emerging graphene-based hybrid coatings have also demonstrated the potential for integrating multiple functionalities, including corrosion resistance and flame retardancy, within environmentally sustainable coating platforms[12]. Advanced multifunctional nanocomposite coatings designed for marine superstructures have demonstrated the importance of hybrid organic-inorganic architectures in improving corrosion resistance and structural durability under saline conditions[13].

To enhance multifunctionality, ZP is often incorporated into natural biopolymers such as cellulose and chitosan [14,15]. Cellulose, the most abundant natural polysaccharide, provides renewable, biodegradable, and mechanically robust matrices with abundant hydroxyl groups for chemical modification [16–18]. Cellulose-based nanocomposites improve adhesion, mechanical reinforcement, and hydrophilicity control in protective coatings[19]. Chitosan, a deacetylated derivative of chitin, expands this potential due to its amino and hydroxyl groups, which interact strongly with metal ions and phosphate species [21]. Importantly, chitosan also possesses inherent antimicrobial activity, making it especially suitable for applications where corrosion and bacterial contamination occur simultaneously. Incorporation of zinc species into chitosan matrices has been reported to yield nanocomposites with improved inhibition efficiency, strong film-forming ability, and antibacterial performance [20–22,24].

Extensive studies have investigated phosphate-based nanocomposites, nanostructured inhibitors, and polymer hybrids for corrosion protection [17,24,25]. Multifunctional polyurethane nanocomposite coatings have also demonstrated enhanced anticorrosion and

mechanical properties through synergistic nanoparticle-polymer interactions[22]. Recent developments in MXene-based nanocomposites have further emphasized the role of two-dimensional hybrid nanomaterials in achieving superior electrochemical barrier performance and multifunctionality[23]. Recently, Liu et al. fabricated Zn-containing MAO coatings on Ti6Al4V with excellent initial antibacterial activity (up to 100%), but the efficacy declined sharply after 14 days of immersion due to rapid Zn^{2+} depletion, and no corrosion protection for mild steel was reported[24]. Yang et al. prepared zinc-phosphate-doped MAO coatings on AZ31B Mg alloys that showed enhanced corrosion resistance and cytocompatibility, yet the coating lacked any antibacterial functionality and was limited to Mg substrates[11]. Cai et al. developed multi-interface structured zinc phosphate particles in waterborne epoxy with outstanding long-term barrier performance (3000 h), but again no antimicrobial activity was integrated. In contrast, the present ZPP-GO@Cu nanocomposite combines, for the first time, a soluble Cu^{2+} source, a PVP-stabilized ion-release matrix, and a GO physical barrier, achieving both sustained high corrosion inhibition (89.2% IE) and complete bacterial eradication (100% kill rate) on mild steel a synergistic multifunctional performance not reported in any of the above studies[25].

To the best of our knowledge, no prior ZnP-based biopolymer system has provided a direct comparative evaluation of cellulose versus chitosan shells within a core–shell architecture for dual corrosion inhibition and antibacterial protection on mild steel. For instance, zinc phosphate–polymer composites have demonstrated self-healing behaviors, while chitosan-based nanocomposites have improved adhesion and functioned as green inhibitors. Antibacterial nanocomposites incorporating zinc or chitosan have also shown effectiveness against biofilm formation and MIC [15,26]. Nevertheless, most existing systems display limited or passive functionality, offering either corrosion resistance or antibacterial action, but rarely both in a synergistic, environmentally responsive manner [26–28].

Moreover, the release behaviors of these nanocomposites under different corrosive conditions neutral, acidic, and alkaline are not well understood, even though steels in service often encounter fluctuating pH and chloride levels [9,14]. This gap restricts the practical applicability of current materials. To address these limitations, the present study investigates zinc-phosphate-cellulose (ZnP@Cel), zinc-phosphate-chitosan (ZnP@Ch), and zinc-phosphate (ZnP) nanoparticles as intelligent nanocomposites for dual corrosion and antibacterial protection.

These nanocomposites are designed to: (1) Respond adaptively to environmental stimuli (pH and chloride ions) encountered in neutral, acidic, and alkaline conditions, (2) Release active inorganic (Zn^{2+}, PO_4^{3-}) and organic species in a controlled manner to inhibit corrosion, (3) Form durable protective passive films on mild carbon steels exposed to 3.5 wt.% NaCl solution, (4) Exhibit antibacterial functionality, leveraging zinc and chitosan's inherent bioactivity [26]. The novelty of this work lies in the integration of multifunctional inorganic–organic nanocomposites that exhibit intelligent, self-regulated, and dual-action behavior. Unlike conventional nanocomposites, the proposed nanocomposites simultaneously mitigate electrochemical corrosion and microbial activity while adapting their release to environmental conditions. This approach advances the design of sustainable, smart protective materials for steels with potential applications in marine, oil and gas, biomedical, and structural industries.

2. Materials and Methodology

2. 1 Raw materials

In this study, zinc nitrate hexahydrate ($Zn(NO_3)_2 \cdot 6H_2O$, Merck), sodium phosphate dodecahydrate ($Na_3PO_4.12H_2O$, Merck), Triton X-100 ($(C_{14}H_{22}O)C_2H_4O)_n$, Sigma–Aldrich), cellulose (microcrystalline, Sigma–Aldrich), and chitosan (medium molecular weight, ≥75% degree of deacetylation, Sigma–Aldrich) were used as the principal precursors. Chitosan was

dissolved in acetic acid (CH_3COOH, Merck), while ethanol (96%, Mojallali Co., Iran) and acetone (Merck) were employed as cleaning solvents.

All chemicals were of analytical grade and applied without further purification. Deionized water was obtained from a Milli-Q system and used throughout all preparations. For electrochemical analyses, rectangular mild steel specimens (ST-12 grade, Mobarakeh Steel Co., Iran) were mechanically polished with abrasive papers (200–800 grit), washed with acetone, and air-dried prior to testing. The chemical composition (wt.%) of ST-12 mild steel is C ≤ 0.10, Mn 0.30–0.45, P ≤ 0.035, S ≤ 0.035, Fe balance. Moreover, rectangular specimens measuring 7.0 × 3.0 × 0.3 cm^3 were used. Prior to immersion testing, the metallic surfaces were selectively masked with a beeswax–colophony barrier coating, leaving a 1 cm × 1 cm exposed working area for EIS measurements.

2. 2 Zinc-Phosphate (ZP) Nanocomposite Fabricating

Zinc phosphate (ZnP) nanoparticles were synthesized via a precipitation method using Triton X-100 as a stabilizer. Approximately 1.2 g of zinc nitrate hexahydrate ($Zn(NO_3)_2.6H_2O$) was dissolved in 100 mL of double-distilled water under continuous stirring until a clear, homogeneous solution was obtained. To this solution, 2 mL of Triton X-100 was added as a non-ionic surfactant [29].

The mixture was stirred vigorously for 30 minutes to ensure the formation of micelles and a uniform environment for nanoparticle nucleation. In a separate beaker, 0.9 g of sodium phosphate dodecahydrate ($Na_3PO_4.12H_2O$) was dispersed in 100 mL of deionized water, yielding a transparent solution with a slightly alkaline pH. The phosphate solution was then added dropwise and slowly into the vigorously stirred zinc nitrate-Triton X-100 solution at room temperature. The phosphate solution was then added dropwise and slowly into the vigorously stirred zinc nitrate-Triton X-100 solution at room temperature, during which the pH

of the reaction mixture was maintained at approximately 7.0–7.5. During this process, the mixture gradually turned cloudy, indicating the nucleation of zinc phosphate particles within the micellar templates. The suspension was kept under magnetic stirring for 2 h to ensure complete reaction and to allow the surfactant to cap the nanoparticles, promoting uniform growth and inhibiting agglomeration [29].

Following this stage, the colloidal mixture was subjected to centrifugation at 10000 rpm for 15 min to separate the precipitated zinc phosphate (ZnP) nanoparticles. The obtained solid fraction was thoroughly rinsed three times with a mixture of ethanol and deionized water to eliminate unreacted ions, by-products, and any residual surfactant. Finally, the washed ZnP precipitate was dried in an oven at 60 °C for 12 h, yielding fine ZnP nanopowder ready for further use.

2. 3 Designing smart Zinc-Phosphate–Chitosan (ZnP@Ch), and Zinc-Phosphate–Cellulose (ZnP@Cel) Nanocomposites

Initially, 0.25 g of microcrystalline cellulose powder was ultrasonically dispersed in 80 mL of deionized water to obtain a stable suspension. Separately, 1.0 g of zinc nitrate hexahydrate ($Zn(NO_3)_2 \cdot 6H_2O$) was dissolved in 50 mL of water under stirring until a clear solution was obtained. Subsequently, 0.75 g of sodium phosphate dodecahydrate ($Na_3PO_4 \cdot 12H_2O$) was dissolved in another 50 mL of water and its pH was adjusted to 6.0 using dilute NaOH. The phosphate solution was then introduced slowly, drop by drop, into the cellulose-containing zinc solution under continuous magnetic stirring.

The addition caused the suspension to gradually become turbid, signifying the precipitation of zinc phosphate nanoparticles along the cellulose matrix [30]. The mixture was further stirred for 2 h at ambient temperature to ensure complete nucleation and uniform coating of cellulose fibers. The resulting composite was separated by centrifugation at 10,000 rpm for 15 min,

rinsed three times with deionized water/ethanol to remove free ions, and dried overnight at 60 °C.

The final powder was designated as ZnP@Cel. Additionaly, to prepare ZnP@Ch, 0.25 g of chitosan was first dissolved in 50 mL of 1% acetic acid solution under magnetic stirring until a transparent polymeric solution was obtained. In parallel, 1.0 g of zinc nitrate hexahydrate was dissolved in 40 mL of water, while 0.75 g of sodium phosphate dodecahydrate was dissolved in 40 mL of water and adjusted to pH 5.5. The phosphate solution was introduced dropwise into the zinc solution under vigorous stirring, forming an initial zinc phosphate sol.

Immediately afterward, the chitosan solution was slowly added to the reaction medium, whereupon the mixture transformed into a viscous suspension with gradual opalescence, indicating successful incorporation of zinc phosphate nanoparticles within the chitosan matrix [24,29]. The reaction was maintained for 3 h at room temperature. The composite was then collected by centrifugation, washed several times with ethanol and deionized water, and oven-dried at 55 °C for 12 h, yielding the ZnP@Ch nanocomposite powder. The biopolymer to ZnP mass ratios (approximately 1:4 for both ZnP@Ch and ZnP@Cel) were systematically optimized by varying the initial precursor concentrations (Zn^{2+}/PO_4^{3-} from 0.005 to 0.02 M, biopolymer from 0.1 to 0.5 g per 100 mL) and evaluating corrosion inhibition efficiency (via EIS, R_{ct}) and antibacterial zone of inhibition. The optimal composition, which gave the highest R_{ct} (for ZnP@Cel) and complete bacterial kill rate (100% for ZnP@Cel), was selected for detailed characterization.

Triplicate syntheses were performed for each nanocomposite (ZnP, ZnP@Ch, and ZnP@Cel). Key characterization results, including XRD peak positions, FTIR band shifts, TEM particle size distribution, and EIS R_{ct} values, showed relative standard deviations (RSD) below 6%, confirming good reproducibility. These polysaccharides are inherently hydroscopic (~40%

w/w chitosan, ~15% w/w cellulose) due to their hydroxyl group funtionallities, which generates a matrix that enhances ion diffusion rates [34,35]. The final yield of the ZnP@Cel and ZnP@Ch nanocomposites (based on the total precursor mass, including zinc nitrate, sodium phosphate, and biopolymer) is approximately 78 ± 4% and 72 ± 5% respectively (n = 3 independent syntheses).

2. 4 Preparation of solutions with liberated inhibitors form ZnP, ZnP@Ch, ZnP@Cel Nanocomposites

To investigate the release characteristics of the synthesized nanocomposites and their subsequent corrosion protection behavior, separate aqueous media were prepared containing zinc phosphate nanoparticles (ZnP), zinc-phosphate–chitosan (ZnP@Ch), and zinc-phosphate–cellulose (ZnP@Cel). This could find applications on ships where biofilm growth under saline conditions would be an issue; accordingly, 0.1 g of nanocomposite powder was dispersed in 100 mL of deionized water containing 3.5 wt.% NaCl to simulate seawater conditions.

The pH of the suspensions was carefully adjusted to the neutral range (7.0–7.5) using dilute hydrochloric acid (0.5 M HCl) and sodium hydroxide (2 M NaOH). Each mixture was continuously agitated for 24 h to facilitate the controlled release of active inhibiting species from the nanocomposite matrix. The resulting supernatant solutions, enriched with liberated agents, were then employed for immersion studies. Mild steel coupons (1 cm^2 exposed area), previously abraded, rinsed, and dried, were immersed in the extract solutions at different exposure intervals. This allowed assessment of the time-dependent corrosion-inhibition performance associated with the released species from ZnP, ZnP@Cel, and ZnP@Ch nanocomposites [30,31]. Furthermore, detailed methodologies corresponding to steel sheet provision (**Section S1.1**) and anti-corrosion assessment of solution containing of ZnP, ZnP@Ch, ZnP@Cel nanocomposites (**Section S1.2**) are comprehensively documented in the

supplementary file. All electrochemical measurements were conducted in triplicate, and the data are expressed as mean ± standard deviation.

2. 5 Anti-Bacterial Activity Experiments of Nanocomposites

The antibacterial potential of zinc phosphate (ZnP), zinc-phosphate–cellulose (ZnP@Cel), and zinc-phosphate–chitosan (ZnP@Ch) nanocomposites was evaluated using three complementary assays: (a) agar diffusion method, (b) MTT cytocompatibility assay, and (c) colony-forming unit (CFU) counting. In fact, in Agar Diffusion Test, two representative bacterial strains were employed: Staphylococcus aureus (ATCC 25923, Gram-positive) and Escherichia coli (ATCC 25922, Gram-negative) [32].

Bacterial suspensions were streaked on Mueller–Hinton agar plates using the swab-plate method. For testing, nanocomposite powders were sterilized under UV light for 20 min. In the first case, 200 mg of each sample was dispersed in 1 mL of sterile water, and 20 µL of the suspension was pipetted onto the agar surface. In the second case, 20 mg of dry powder was directly applied. Plates were incubated for 24 h at 37 °C, and the diameter of the inhibition zones was measured to quantify antibacterial efficiency [33].

Moreover, in MTT Assay (Cytocompatibility), Cytotoxicity was examined using the L929 fibroblast cell line. Sterilized nanocomposite powders were suspended in phosphate-buffered saline (PBS) and diluted to three concentrations: 50, 100, and 200 µg/mL. Aliquots were introduced into 96-well plates containing 1×10^4 cells/well in DMEM (Sigma) supplemented with 10% fetal bovine serum (FBS) and 1× antibiotic–antimycotic solution (Gibco). Control wells received only the diluent. After incubation at 37 °C with 5% CO_2 for 24 h, 10 µL of MTT solution (0.5 mg/mL) was added to each well and incubated for another 4 h. Subsequently, 100 µL of DMSO was used to dissolve formazan crystals, and absorbance was measured at 570 nm with a microplate reader (Wareness Technology). All tests were performed in triplicate.

Finally, in Colony-Forming Unit (CFU) Assay, Streptococcus mutans (ATCC 35668) was cultured in Lysogeny Broth (LB) medium, and bacterial suspensions were standardized to 1×10^5 CFU/mL. A total of 0.1 g of each nanocomposite powder was incubated in bacterial suspension for 24 h at 37 °C. Serial dilutions (10^{-1}–10^{-10} M) were prepared and spread onto Plate Count Agar (Merck, Germany). Plates were incubated for 48 h at 37 °C, after which visible colonies were counted to determine bacterial survival rates compared with untreated controls. [32]

2. 6 Characterization and Apparatus

FTIR analysis was performed using a PerkinElmer Spectrum 3 spectrometer (USA) to examine the chemical reactions and the formation of ZnP, ZnP@Cel, and ZnP@Ch nanocomposites. XRD measurements (Rigaku, Cu $K\alpha_1$ radiation, $\lambda = 1.54060$ Å, $\Delta 2\theta = 0.04°$, $\Delta t = 1$ s) were conducted to identify the crystalline phases present in the nanocomposites. Morphological and compositional characterization was carried out using FESEM (MIRA3 TESCAN, Czech Republic) equipped with quantitative EDS and qualitative elemental mapping to analyze the smart ZnP, ZnP@Cel, and ZnP@Ch nanocomposites. In addition, high-resolution TEM imaging (Philips EM 208S, 100 kV, Netherlands) was employed to investigate the detailed morphology of ZnP, ZnP@Cel, and ZnP@Ch nanocomposites.

3. Results and Discussion

3. 1 Nanocomposite Analysis

3. 1. 1 FTIR Assesment

Figure 1 compiles infrared fingerprints for pristine zinc phosphate and its cellulose- and chitosan-based hybrids (ZnP@Cel and ZnP@Ch). A wide, structured envelope centered in the 3200–3600 cm^{-1} region appears in all samples, a hallmark of extensive hydrogen bonding among hydroxyl groups and, in the ZnP@Ch hybrid nanocamposite, overlapping N–H

stretches. Subtle band shifts here reflect interactions between biopolymer donors and the phosphate surface. The organic character of the two hybrids is further marked by weak aliphatic C–H stretches near 2925/2850 cm^{-1}. Moving to lower wavenumbers, the ZnP@Ch hybrid nanocamposite presents the expected amide/N–H bending features (1650–1550 cm^{-1}), whereas ZnP@Cel hybrid nanocamposite shows carbonate/oxidized-cellulose shoulders and the ubiquitous water deformation near 1640 cm^{-1}. In the 1460–1200 cm^{-1} span, polysaccharide vibrations (C–H bending; C–O and C–N modes) add complexity to the spectra [39,40]. The spectral core of zinc phosphate lies between 1130 and 900 cm^{-1}, where strong PO_4 stretching and Zn–O–P modes dominate [36]. These intense absorptions are preserved in both hybrids, demonstrating that the phosphate framework remains intact after integration with the biopolymers (**Figure 1 (a)**). The cellulose hybrid also displays its glycosidic C–O–C and C–O stretches (1160 and 1030 cm^{-1}), partially overlapping the phosphate envelope. Finally, bands in the 650–500 cm^{-1} region correspond to O–P–O bending and Zn–O lattice vibrations, again confirming the presence of the inorganic phase (**Figure 1 (b)**) [37]. Collectively, the coexistence of phosphate and polysaccharide signatures, together with modest band shifts, supports a picture of interfacial hydrogen bonding/coordination without disruption of the ZnP network.

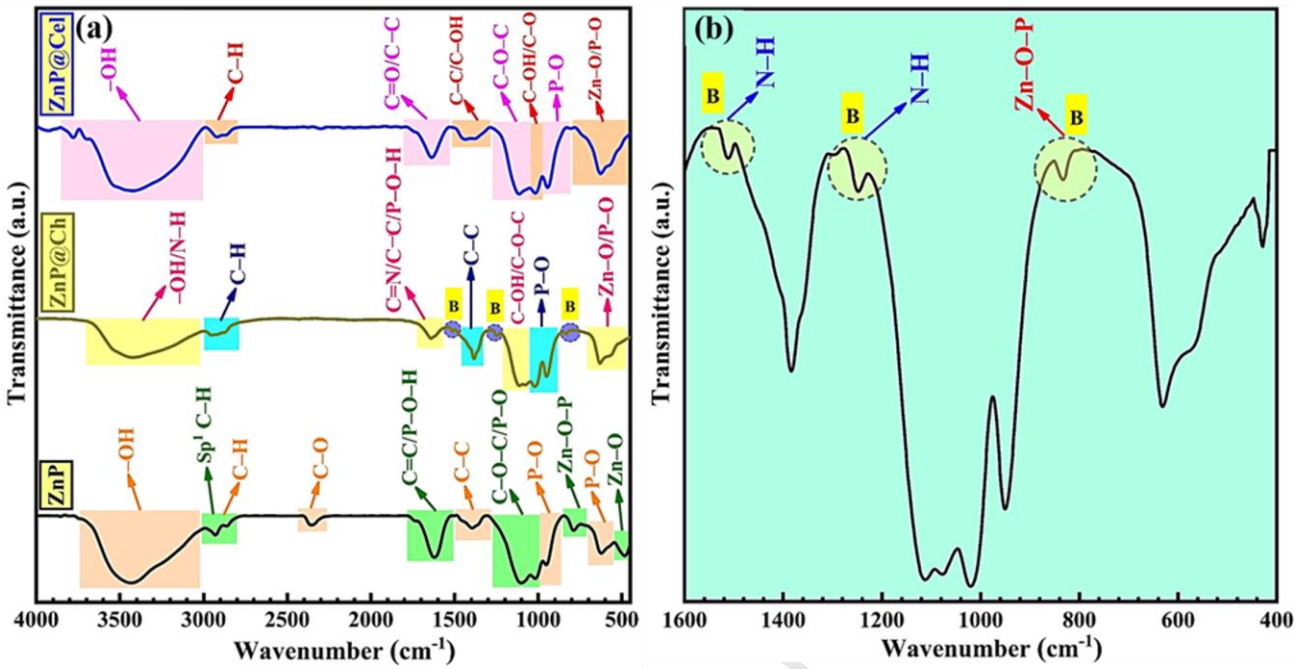

Figure 1. The (a) FTIR spectrum of ZnP, ZnP@Cel, and ZnP@Ch nanocomposites, (b) Exaggarated the finger print region of FTIR of ZnP@Ch nanocomposite.

The **Figure 2** of FTIR spectral shifts provide compelling evidence for the successful synthesis of ZnP@Ch and ZnP@Cel nanocomposites via distinct interfacial mechanisms. For ZnP@Ch, a pronounced bathochromic shift of 44 cm^{-1} in the Zn–O–P vibrational band (**Figure 2 (a)**) in indicates strong interfacial interactions between zinc phosphate nanoparticles and the chitosan matrix. This shift is attributed to coordination between Zn^{2+} centers in zinc phosphate and Lewis-basic functional groups (–NH_2 and –OH) of chitosan, which alters the local electronic environment of the Zn–O–P framework. In addition, a concomitant 23 cm^{-1} shift in the aromatic C–C stretching vibration of chitosan (**Figure 2 (b)**) further supports the presence of interfacial coordination and hydrogen-bonding interactions, confirming effective integration of zinc phosphate nanoparticles within the biopolymer network [38,39].

Conversely, integration in ZnP@Cel is dominated by hydrogen bonding, as evidenced by a 13 cm^{-1} displacement of the glycosidic C–O–C band (**Figure 2 (c)**), characterizing the ether

oxygen as a proton acceptor, and a corroborating 17 cm^{-1} shift in the C–C skeletal vibration (**Figure 2 (d)**) that signifies altered intramolecular forces from surface adsorption [40].

In ZnP@Ch and ZnP@Cel, specific coordination interactions between Zn^{2+} centers and Lewis-basic functional groups of the biopolymer matrix, together with hydrogen bonding involving phosphate oxygen atoms, establish robust interfacial bridges between the inorganic nanoparticles and the organic phase. These dynamic and partially reversible interactions confer environmental sensitivity to the nanocomposites, particularly with respect to changes in pH and ionic strength, which can modulate interfacial bonding, nanoparticle dispersion, and overall stability. Such chemically adaptive behavior underlies the designation of these systems as intelligent nanomaterials, as their structural integrity and functional performance are governed by stimulus-dependent interfacial interactions rather than by externally applied physical fields [26].

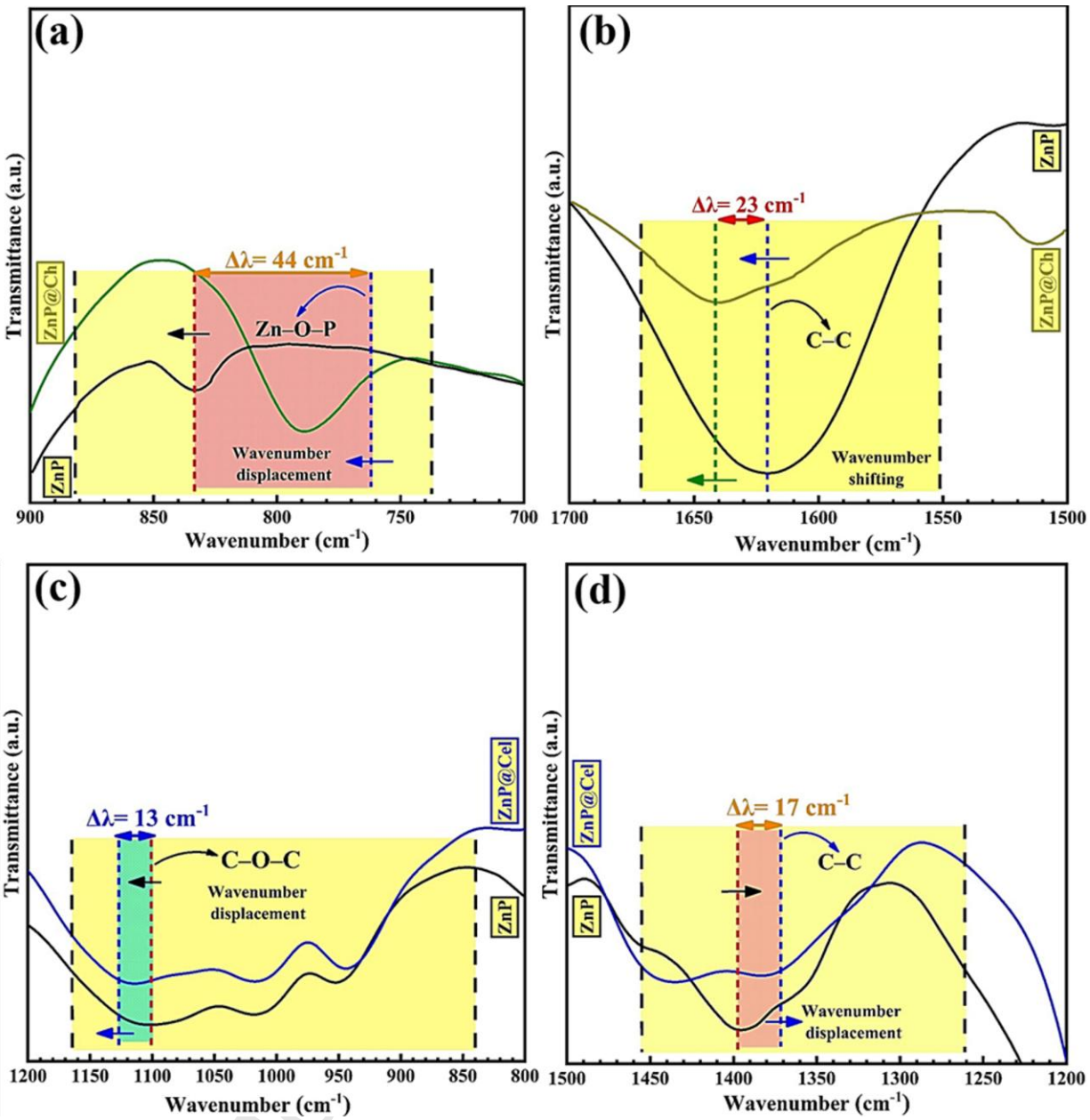

Figure 2. The FTIR spectrums of molecular interactions for intelligent ZnP, ZnP@Cel, and ZnP@Ch nanocomposites, (a) Zn–O–P, (b) stretching C–C, (c) C–O–C, (d) C–C bonds.

3. 1. 2 XRD Assesment

Figure 3 presents the X-ray diffraction (XRD) patterns elucidating the crystalline phase and structural characteristics of the pristine ZnP, ZnP@Cel, and ZnP@Ch nanocomposites. The diffractogram for pristine ZnP exhibits sharp, well-defined peaks indexed to the (104), (101), ($\bar{2}$10), (220), (131), (311), ($\bar{3}$21), and (250) planes, which are unequivocally assigned to a

crystalline $Zn_3(PO_4)_2$ phase (#JCPDS card no. 00-029-1390) [41,42]. In the ZnP@Cel composite, these characteristic crystalline peaks remain distinctly visible, confirming the retention of the zinc phosphate crystal structure; however, they are superimposed on a broad, amorphous halo and a notably elevated background, which is diagnostic of the presence of amorphous cellulose (**Figure 3 (a)**). This same phenomenon is observed even more prominently in the ZnP@Ch pattern, where the sharp $Zn_3(PO_4)_2$ reflections including the (220) plane is clearly evident against an intense amorphous background originating from the chitosan matrix, a well-documented feature of this biopolymer (**Figure 3 (b)**).

The coexistence of these sharp crystalline signatures with the broad amorphous scattering provides definitive evidence for the successful formation of both ZnP@Cel, and ZnP@Ch nanocomposites, wherein crystalline $Zn_3(PO_4)_2$ nanoparticles are effectively dispersed and stabilized within the organic biopolymer networks without undergoing phase change, thereby creating a hybrid semi-crystalline stable ZnP@Cel, and ZnP@Ch nanocomposite structure critical for the material's properties [43].

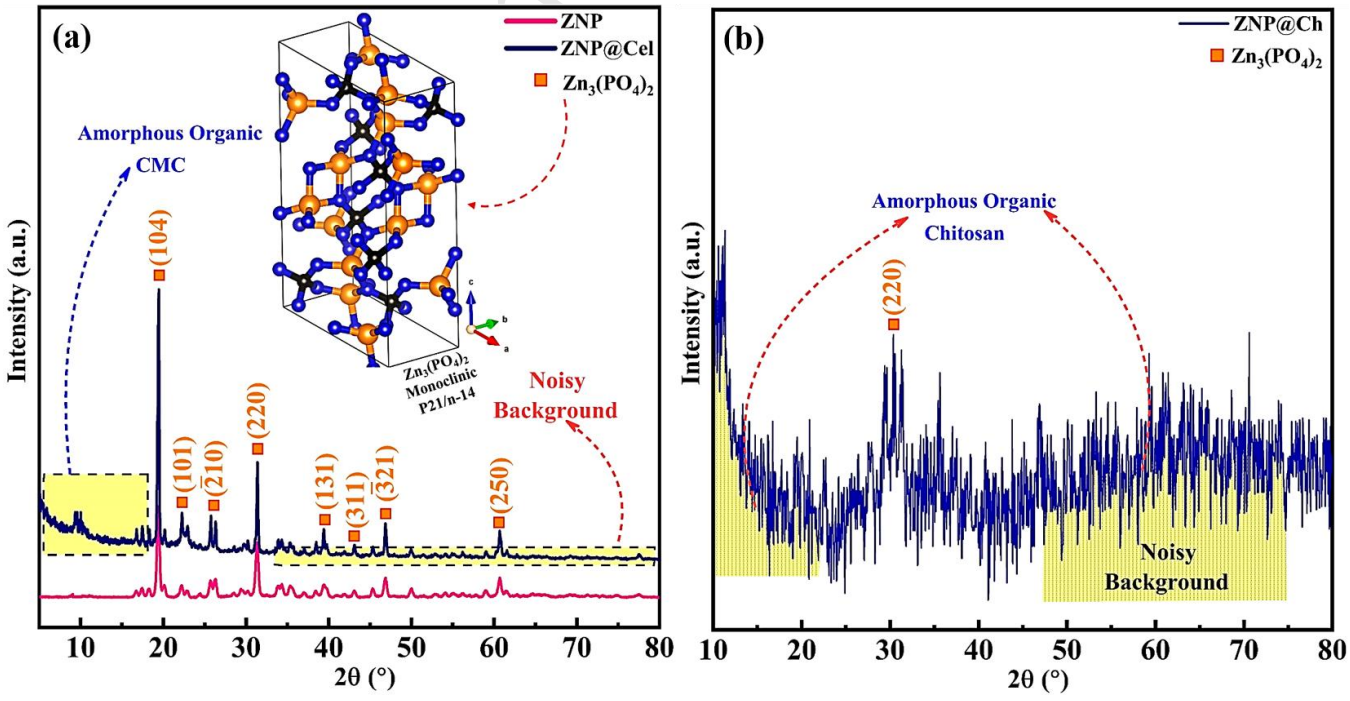

Figure 3. The XRD patterns of (a) ZnP, and hybrid ZnP@Cel, (b) ZnP@Ch nanocomposites. In the unit cell zinc are the orange atoms, oxygen the red and phosphorous the black atoms

Using the Scherrer relation ($D=K\lambda/\beta\cos\theta$), the average crystallite sizes of the $Zn_3(PO_4)_2$ phase (based on the (220) reflection at $2\theta = 31.5°$) were calculated as 15.8 nm for pristine ZnP, 15.0 nm for ZnP@Ch, and 14.0 nm for ZnP@Cel[23,49]. The crystallinity indices, estimated from the integrated intensity ratio of crystalline peaks to total scattered intensity, were approximately 78% for ZnP, 65% for ZnP@Ch, and 60% for ZnP@Cel. Interestingly, the corrosion inhibition efficiency inversely correlates with crystallinity and crystallite size: ZnP (highest crystallinity, 15.8 nm) showed the lowest IE (30.8%), while ZnP@Cel (lowest crystallinity, 14.0 nm) exhibited the highest IE (75.3%). This trend indicates that smaller crystallites and reduced crystallinity, associated with the amorphous biopolymer matrices, facilitate more efficient Zn^{2+} and PO_4^{3-} release, promote uniform film formation, and enhance the barrier performance. The cellulose shell in ZnP@Cel provides an optimal balance of ion-release kinetics and physical encapsulation, resulting in superior corrosion protection[7,25].

3. 1. 3 Morphological Aparaisment of hybrid ZnP, ZnP@Cel, and ZnP@Ch nanocomposites

Figure 4 presents high-resolution FESEM micrographs and corresponding EDS elemental maps of the synthesized ZnP, ZnP@Ch, and ZnP@Cel nanocomposites. The FESEM analysis revealed distinct morphological differences between the samples. The pristine ZnP nanoparticles (**Figure 4 (a_1, b_1)**) exhibited a tendency to form spherical agglomerates, with a calculated average particle size of 36.3 nm, a typical characteristic of inorganic precipitates with high surface energy [44,45].

The functionalization with biopolymers markedly influenced the microstructure. The ZnP@Ch nanocomposite (**Figure 4 (a_2, b_2, c_2)**) displayed an assembled, layered-spherical architecture

with an increased average size of 52.3 nm, indicating that the chitosan polymer matrix effectively templated the growth and assembly of the ZnP particles [21,28].

Similarly, the ZnP@Cel nanocomposite (**Figure 4 (a_3, b_3, c_3)**) formed uniform, hybrid structures characterized as agglomerated semi-spherical particles, with the largest average size of 64.4 nm. This suggests a strong interaction between the cellulose fibrils and the inorganic phase, leading to a coherent and homogenously structured nanocomposite material [22,46].

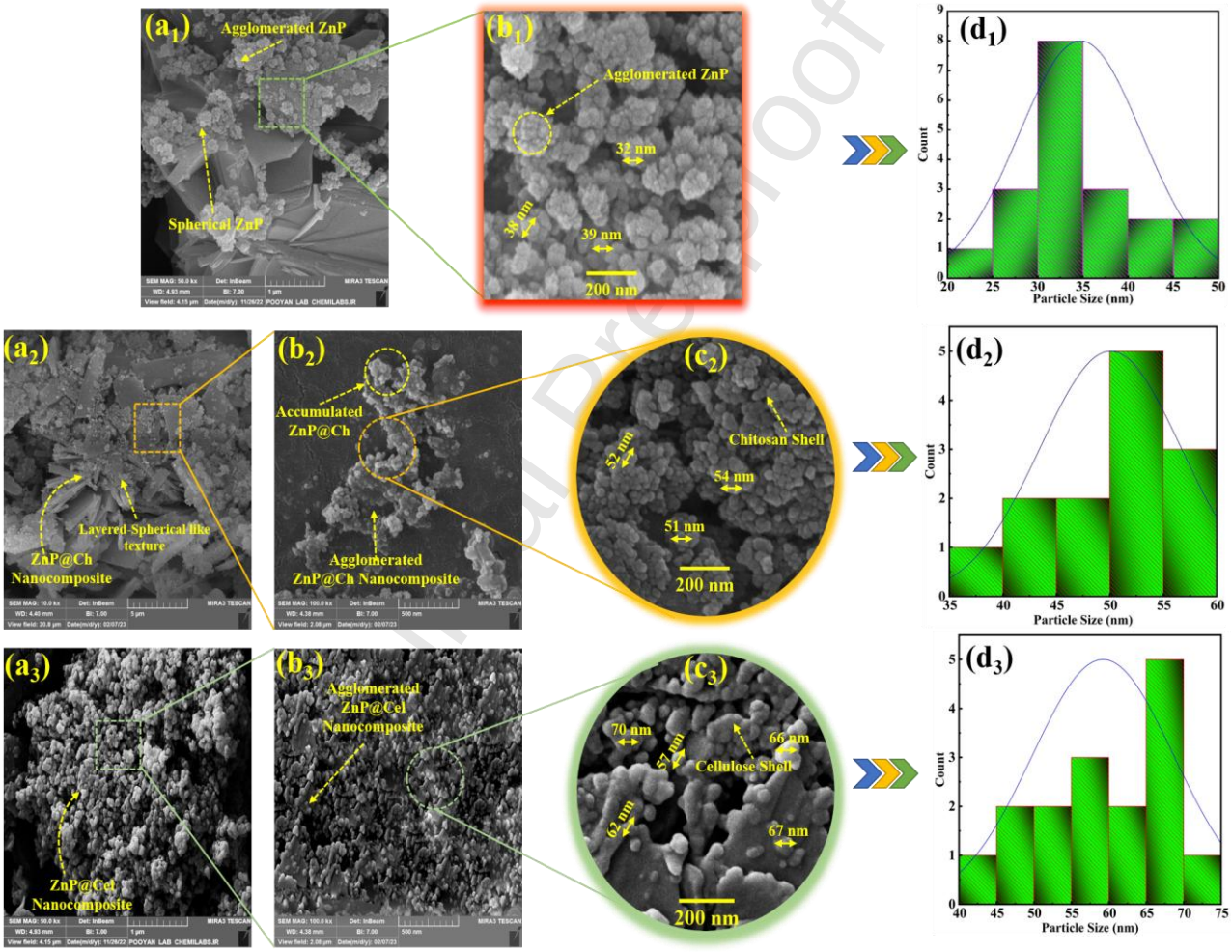

Figure 4. High-resolution FESEM micrographs at different magnifications (10, 50, and 100 kx) of the synthesized ZnP, ZnP@Cel, and ZnP@Ch nanocomposites with particle size distribution histograms: (a_1,b_1, d_1) agglomerated ZnP particles, (a_2,b_2,c_2,d_2) assembled hybrid ZnP@Ch, and (a_3,b_3,c_3,d_3) uniformly assembled hybrid ZnP@Cel nanocomposites.

Agglomeration analysis revealed distinct differences among the samples. Pristine ZnP nanoparticles exhibited the highest degree of agglomeration, forming dense, irregular clusters due to the high surface energy and lack of a stabilizing organic shell. In contrast, ZnP@Ch and ZnP@Cel showed significantly reduced agglomeration, with the biopolymer shells providing steric stabilization and preventing extensive particle aggregation. The cellulose shell in ZnP@Cel appeared to offer the most effective dispersion, as evidenced by the more uniform spatial distribution of particles in the FESEM images (Figure 4), which correlates with its superior corrosion inhibition performance and higher R_{ct}. The reduced agglomeration in biopolymer-modified samples enhances the effective surface area available for ion release and film formation, contributing to the improved barrier properties[10,11].

In the **Figure 5 (a_1-c_3),** the EDS elemental mapping and quantitative analysis provided definitive evidence for the successful formation of these hybrid nanocomposites. The elemental distribution for ZnP@Ch confirmed the incorporation of organic material through the presence of C (24.01 wt%.) and N (4.67 wt%.), elements inherent to the chitosan polymer which suggests that 54% by mass of this composite material is inorganic which would increase the release of Zn^{2+} to the surrounding environment. Likewise, the ZnP@Cel composite showed a significant C content (22.60 wt%.) attributable to cellulose, with no nitrogen detected, consistent with its chemical structure [24,47], which suggest 1.41% by mass higher content of the inorganic phase which suggests similar capacity of Zn^{2+} to that of chitosan, in the absence of the polymer matrix effect on ion diffusion. The uniform spatial distribution of all detected elements (Zn, O, P, C) across the mapped areas in both hybrid ZnP@Cel, and ZnP@Ch nanocomposites confirm the homogeneous integration of the biopolymer and inorganic phases at the microscopic level, rather than a mere physical mixture.

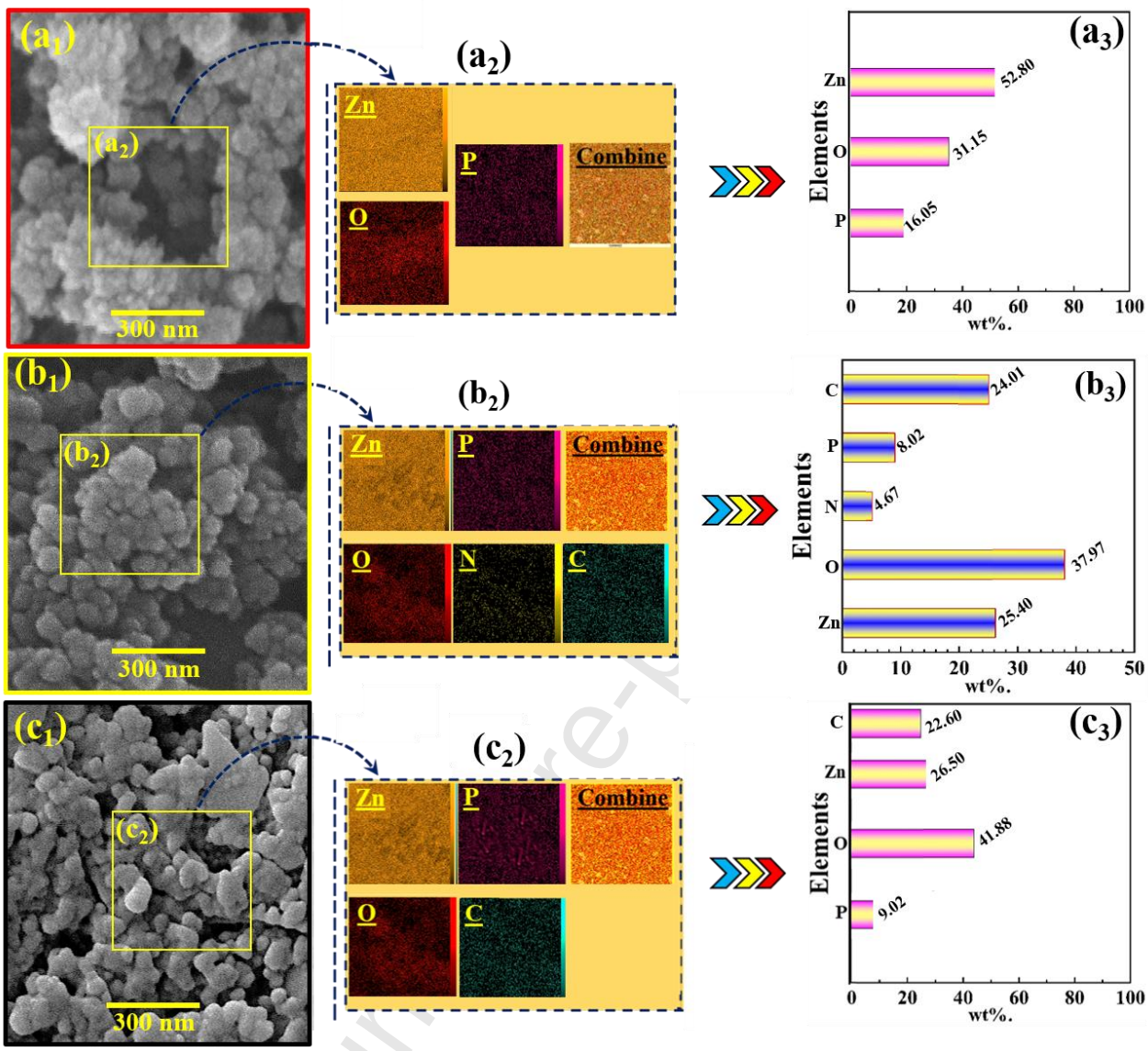

Figure 5. The elemental distribution of EDS Mapping of novel ZnP, ZnP@Cel, and ZnP@Ch nanocomposites; **(a_1,a_2,a_3)** ZnP, (**b_1,b_2,b_3**) ZnP@Ch, (**c_1,c_2,c_3**) ZnP@Cel nanocomposite.

3. 1. 4 TEM Investigation of ZnP, ZnP@Cel, and ZnP@Ch nanocomposites

Figure 6 revealed the high resolution TEM images of ZnP, ZnP@Cel, and ZnP@Ch nanocomposites. The TEM micrographs reveal well-dispersed spherical nanoparticles with an average diameter of 36.25 nm, consistent with FESEM findings. The relatively uniform contrast and distinct outlines confirm the inorganic crystalline nature of ZnP and its tendency to form solid spherical morphologies (**Figure 6 (a_1,b_1)**). The ZnP@Ch nanocomposite presents

semi-dispersed spherical nanoparticles with an average size of 51.5 nm. The TEM confirms the presence of a thin, uniform chitosan shell (4 nm thickness) surrounding the ZnP cores [28,48,49]. The consistent shell contrast demonstrates effective embedding of ZnP within the chitosan framework. This morphology indicates a robust composite structure where chitosan contributes not only to stabilization but also potential antibacterial properties (**Figure 6 (a_2,b_2)**) [22,50].

The hybrid ZnP@Cel nanocomposite shows larger, agglomerated spherical particles with an average size of 61.5 nm. The TEM images clearly display a thin, continuous organic shell (5.25 nm thick) encapsulating the inorganic ZnP core [46,51]. This shell originates from the cellulose matrix and appears to coat the ZnP particles uniformly, suggesting strong interfacial interactions and an integrated core–shell architecture. Such encapsulation is consistent with FESEM observations and reflects the ability of cellulose to wrap and stabilize the nanoparticles (**Figure 6 (a_3,b_3)**). Ulimately, the TEM results corroborate FESEM findings, validating the spherical morphology, core–shell architecture, and dimensional consistency across the ZnP, ZnP@Cel, and ZnP@Ch systems. The cellulose and chitosan-derived shells play a key role in regulating particle size, preventing extensive aggregation, and adding corrosion inhibition accompanied with antibacterial properties [58,59].

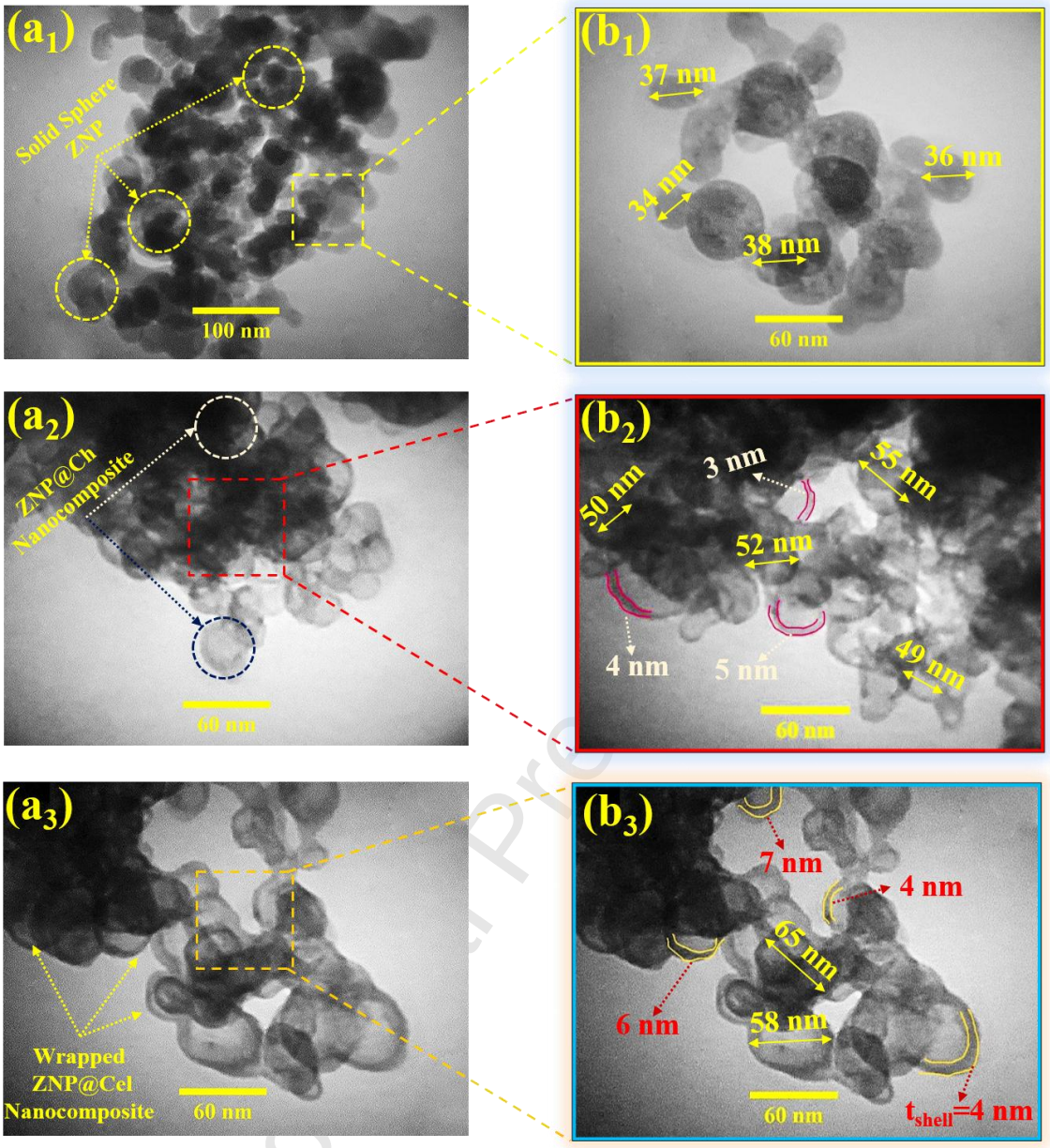

Figure 6. The TEM images of ZnP **(a_1,b_1)**, ZnP@Ch **(a_2,b_2)**, and ZnP@Cel **(a_3,b_3)** nanocomposites with distinct morphological features and contrast variations.

While the current TEM analysis at 100 kV resolution clearly reveals the core–shell morphology, nanoparticle distribution, and interfacial integration, direct observation of atomic-scale crystal defects (e.g., dislocations, vacancies) was not possible with the available instrument. Such defects could potentially accelerate the controlled release of Zn^{2+} ions, contributing to the observed corrosion inhibition and antibacterial performances[35,50,60].

Future work employing spherical-aberration-corrected HRTEM and electron energy loss spectroscopy (EELS) is planned to elucidate the defect structure–ion release relationship. Furthermore, zeta potential measurements, which would provide valuable insight into colloidal stability and surface charge, were not performed in this study. Future work employing spherical-aberration-corrected HRTEM and electron energy loss spectroscopy (EELS) is planned to elucidate the defect structure–ion release relationship, and zeta potential characterization will be included to correlate surface charge with dispersion stability and antibacterial adhesion.

3. 2 Electrochemical and Anti-Corrosion Assessment of Nanocomposites

3. 2. 1 PDP Analysis & Corrosion Prevention Mechanisms

The **Figure 7** and **Table 1** demonstrated the normal accompanied by shifted Potentiodynamic Polarization (PDP) curves and vital electrochemical parameters for mild steel panels after 24 h immersion in corrosive saline solution without (Blank) and with ZnP, ZnP@Ch, and ZnP@Cel nanocomposites, respectively.

The PDP curves and corresponding electrochemical parameters provide valuable insights into the corrosion mitigation behavior of ZnP, ZnP@Cel, and ZnP@Ch nanocomposites on mild steel surfaces. The blank sample immersed in 3.5 wt% NaCl exhibited an $-E_{corr}$ of 660 mV (vs. SCE) and a relatively high corrosion current density (i_{corr} = 7.12 µA/cm²), which reflects the aggressive chloride-induced dissolution of steel in the absence of protective inhibitors [52,53]. Upon the introduction of ZnP nanocomposites, a notable positive shift in $-E_{corr}$ to 587 mV was observed, along with a modest reduction of i_{corr} to 4.93 µA/cm².

This behavior could be attributed to the precipitation of insoluble Zn–P species on the steel surface, which forms an initial protective anodic $Fe^{2+/3+}$–P pluging film that partially retards anodic dissolution [15,19]. The inhibition efficiency, however, was limited to 30.8%

(according to the **Equation 1**)), suggesting that the ZnP coating alone provides an incomplete barrier against chloride ingress due to possible film porosity and lack of organic reinforcement [41].

$$\%IE_i = 100 \times \left(1 - \frac{i_{corr,Nanocomposites\ presence}}{i_{corr,Blank}}\right) \quad \textbf{(1)}$$

The more effective corrosion protection was observed for ZnP@Ch nanocomposites. The system demonstrated a significant shift in $-E_{corr}$ to 600 mV, a reduction in i_{corr} to 3.85 µA/cm², and the highest inhibition efficiency of 45.9%. These superior results can be directly linked to the chitosan shell structure. Chitosan, a biopolymer rich in amine and hydroxyl groups, not only wraps ZnP cores in a uniform shell (4 nm thickness as verified by TEM results) but also exhibits intrinsic corrosion inhibition properties [49,54].

Its functional groups facilitate strong adsorption onto the steel surface through coordination with Fe^{2+}/Fe^{3+} ions, forming a compact organic–inorganic interphase. This interaction enhances the stability and impermeability of the protective layer, thereby effectively suppressing both anodic and cathodic electrochemical reactions [55,56]. The drastic increase in the anodic slope (βa = 111 mV/dec) combined with significant modification of the cathodic slope (–βc = 236 mV/dec) provides evidence for a synergistic mixed-type inhibition mechanism [57]. Specifically, ZnP@Ch reduces anodic metal dissolution by reinforcing phosphate $Fe^{2+/3+}$–P film deposition, while simultaneously hindering cathodic oxygen reduction through the blocking action of chitosan-derived complexes [58].

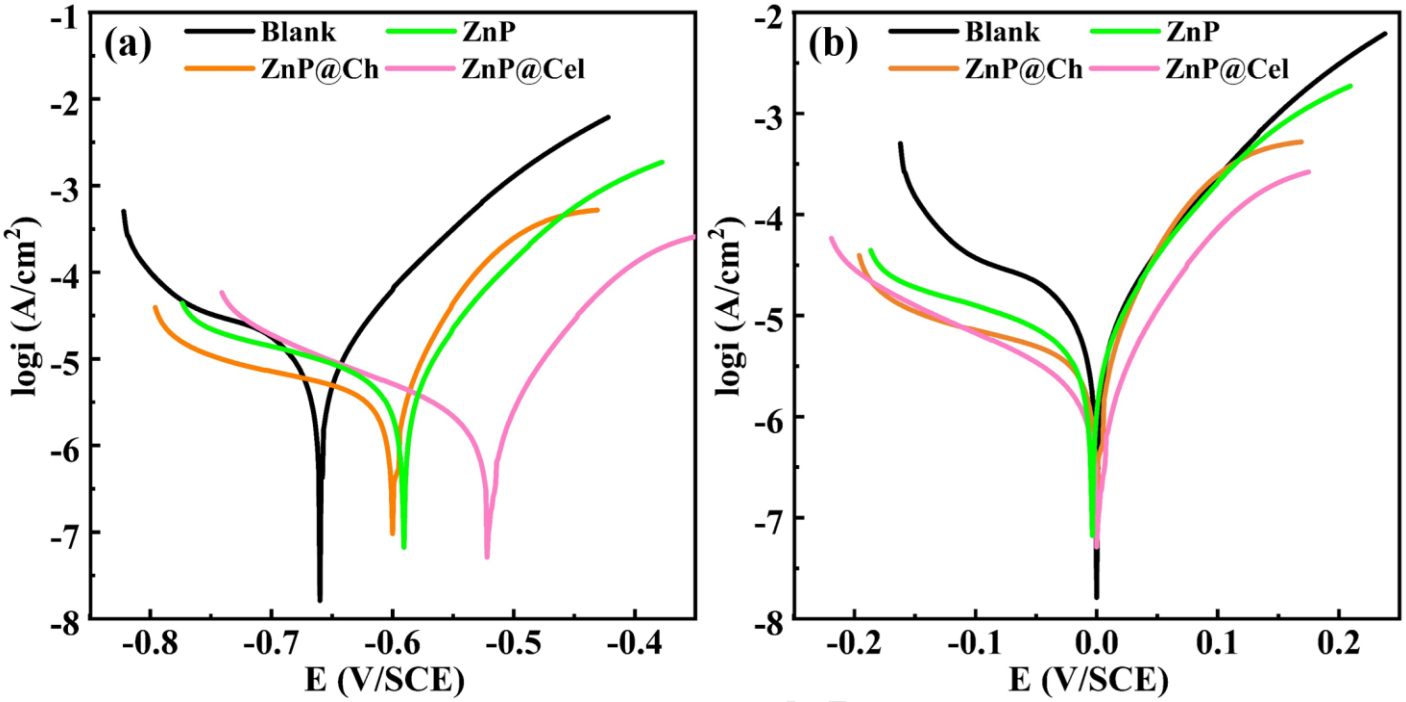

Figure 7. Evans diagrams obtained PDP measurements of mild steel specimens exposed for 24 h to 3.5 wt% NaCl solution in the absence and presence of ZnP, ZnP@Ch, and ZnP@Cel nanocomposites; (a) standard representation and (b) potential-shifted representation.

A most pronounced protective effect was achieved with ZnP@Cel nanocomposites, where -E_{corr} shifted positively to 522 mV and i_{corr} decreased substantially to 1.76 µA/cm². The calculated inhibition efficiency increased to 75.3 %, accompanied by a significant enhancement in polarization resistance. The corrosion rates (CR) were calculated from the corrosion current densities using the standard **Equation (2)**:

$$CR = \frac{i_{Corr} \times K \times E_W}{\rho \times A}) \qquad \textbf{(2)}$$

where i_{corr} is the corrosion current density, K is a constant (3272 mm.A^{-1}.cm^{-1}.year^{-1}), E_W is the equivalent weight of iron (27.92 g/mol), ρ is the density of iron (7.87 g/cm³), and A is the area (1 cm²) The calculated corrosion rates are 0.132 mm/year for the blank, 0.091 mm/year for ZnP, 0.071 mm/year for ZnP@Ch, and 0.033 mm/year for ZnP@Cel, confirming the significant reduction in corrosion rate upon addition of the nanocomposites[69,70].

The TEM and FESEM findings corroborate this performance by showing a uniform 5 nm cellulose shell enveloping the ZnP cores.

The cellulose matrix contributes to the formation of a dense, adherent, and hydrophilic interfacial layer that limits chloride penetration, while simultaneously improving film compactness [46,51]. The moderate reduction in both anodic and cathodic Tafel slopes suggests that ZnP@Cel exerts its inhibition effect through a mixed mechanism, wherein the cellulose-derived organic functionalities enhance physical encapsulation and chemical bonding with the steel substrate [59]. The systematic improvement in electrochemical behavior from Blank < ZnP < ZnP@Ch < ZnP@Cel underscores the role of biopolymer functionalization in enhancing the effectiveness of phosphate-based nanocomposites. These trends can be interpreted as a result of the relative water content of the coating, with cellulose having a smaller water content than chitosan which decrease the rate of ion diffusion and consequently corrosion in aqueous saline environments.

The chitosan shell improves dispersion and mechanical stability, whereas the cellulose shell provides both structural encapsulation and additional active sites for electrochemical interaction with the steel substrate [58]. The combined effects translate into more compact, adherent, and durable protective layers that resist chloride-induced attack.

Ultimately, the PDP outcomes affirm that ZnP@Cel, ZnP@Ch and ZnP nanocomposites deliver the highest degree of corrosion resistance, respectively, making them promising candidates for advanced eco-friendly corrosion inhibitors that exploit synergistic inorganic–organic interactions at the nanoscale.

Table 1. Experimentally obtained and theoretically PDP parameters with corrosion rate calculation outcomes for mild steel sheets after 24 h immersion in a 3.5 wt% NaCl solution

(blank) in comparison with the protective performance of novel ZnP, ZnP@Ch, and ZnP@Cel nanocomposites.

[a] The standard deviation varied from 3.1% to 5.6%.

[b] The standard deviation varied from 1.2% to 2.1%.

Sample	$-E_{corr}$[a] (mV/SCE)	β_a[b] (mV/decade)	$-\beta_c$[c] (mV/decade)	i_{corr}[d] ($\mu A/cm^2$)	IE_i[f] (%)	CR (mm/year)
Blank	660	76 ± 0.1	316 ± 0.63	7.12	-	0.132
ZnP	587	125 ± 0.21	312 ± 0.74	4.93	30.8	0.091
ZnP@Ch	600	111 ± 0.13	236 ± 0.81	3.85	45.9	0.071
ZnP@Cel	522	289 ± 0.32	581 ± 0.92	1.76	75.3	0.033

[c] The standard deviation varied from 1.3% to 2.8%.

[d] The standard deviation varied from 2.1% to 3.1%.

[e] The standard deviation varied from 5.1% to 6.1%.

[f] The standard deviation varied from 2.1% to 3.6%.

3. 2. 2 Mechanistic Interpretation of Corrosion Inhibition

To further clarify the superior inhibition efficiency observed for ZnP@Cel and ZnP@Ch nanocomposites, a schematic illustration of their protective action is presented in Figure 8. The mechanism involves the formation of a hybrid organic–inorganic interfacial layer, where the ZnP core and the polymeric shell (cellulose or chitosan) synergistically suppress both anodic metal dissolution and cathodic oxygen reduction.

In the ZnP@Ch system, the protonated amino and hydroxyl groups of chitosan strongly coordinate with Fe^{2+}/Fe^{3+} ions on the steel surface, forming chelated complexes that act as an

electrochemical barrier and inhibit charge transfer. Simultaneously, the ZnP phase contributes phosphate and zinc ions that promote the deposition of a compact Fe–Zn–P protective film.

In contrast, the ZnP@Cel nanocomposite primarily operates through physical encapsulation and hydrogen bonding. The cellulose shell forms a dense hydrophilic matrix that enhances adhesion, limits electrolyte uptake, and stabilizes the deposited phosphate film. This dual mechanism of chemical adsorption (ZnP@Ch) and physical sealing (ZnP@Cel) effectively blocks both anodic and cathodic reaction sites, resulting in the remarkable inhibition efficiencies evidenced by PDP and EIS analyses. The distinct electrochemical barrier performance of ZnP@Cel compared to ZnP@Ch can be explained by the different interfacial interactions governing each system. In ZnP@Ch, the protonated amino and hydroxyl groups of chitosan strongly coordinate with Fe^{2+}/Fe^{3+} ions on the steel surface, forming chelated complexes that act as an electrochemical barrier and inhibit charge transfer. This coordination bonding creates a chemically anchored protective layer[36,70]. In contrast, ZnP@Cel primarily operates through physical encapsulation and hydrogen bonding. The cellulose shell forms a dense hydrophilic matrix that enhances adhesion, limits electrolyte uptake, and stabilizes the deposited phosphate film[72]. The stronger hydrogen-bonding network in cellulose, as evidenced by FTIR analysis, creates a more cohesive and stable shell that protects the ZnP core while allowing controlled ion diffusion. Furthermore, the lower water content of cellulose (15% w/w) compared to chitosan (40% w/w) results in a more stable matrix that resists excessive swelling and maintains structural integrity, preventing rapid ion depletion and maintaining barrier performance over extended immersion. Thus, the superior barrier performance of ZnP@Cel arises from a combination of physical sealing, superior matrix stability, and sustained ion-release passivation[73].

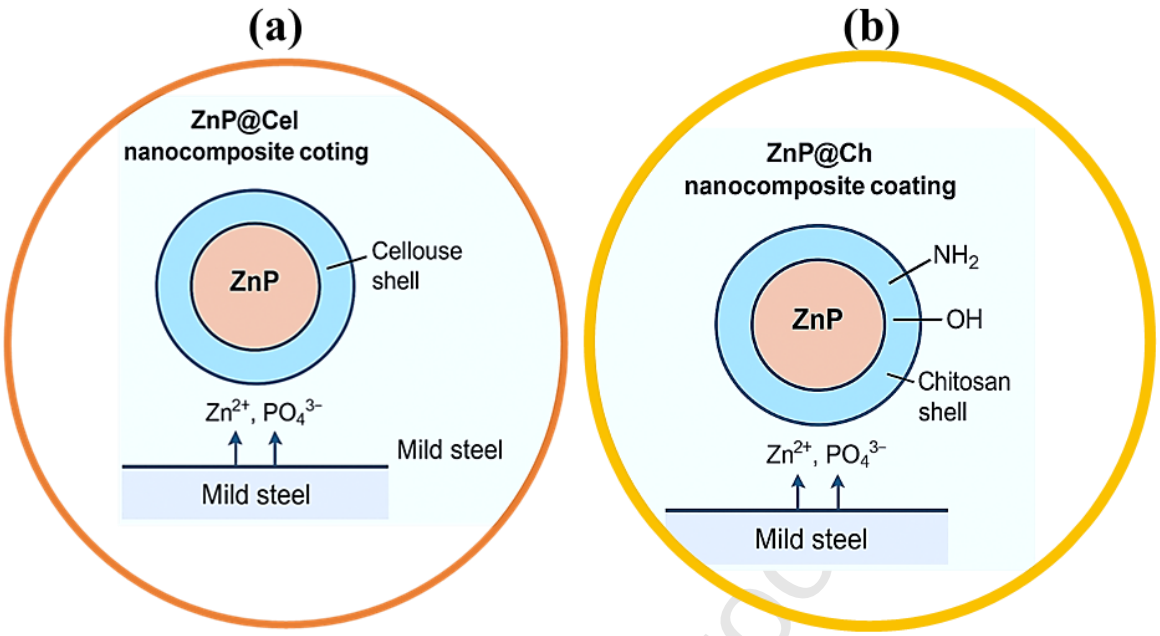

Figure 8. Proposed corrosion inhibition mechanism for (a) ZnP@Cel and (b) ZnP@Ch nanocomposite coatings.

The proposed mechanism (Figure 8) demonstrates that ZnP@Cel forms a dense, adherent organic–inorganic barrier through both physical encapsulation and chemical adsorption, whereas ZnP@Ch achieves effective corrosion suppression through coordination bonding and mixed-type inhibition behavior.

Table 2. Literature-reported oxygen permeability coefficients (P) of cellulose, chitosan, and representative polymeric materials under standard temperature and pressure (STP; T = 273.15 K, P = 1 atm) used as reference values to support the proposed oxygen-barrier mechanism of ZnP@Cel and ZnP@Ch nanocomposites [74,75].

Material	**O_2 Permeability** $\times 10^{-10}$ $cm^3 \cdot cm/(cm^2 \cdot s \cdot cm\ Hg)$	**O_2 Permeability relative to water**
Water	~3000	Reference (100%)
Chitosan (dry)	0.05-0.5	0.002-0.02%

Cellulose	0.001-0.01	0.0003-0.003%
Epoxy resin	0.5-5	0.02-0.17%
Polyurethane	5-20	0.17-0.67%
LDPE	200-300	6-10%
Natural rubber	1500-2000	50-67%

Furthermore, literature-reported oxygen permeability data (Table 2) indicate that cellulose and chitosan possess substantially lower oxygen permeability than many conventional polymeric coating materials. Although oxygen permeability was not experimentally measured in the present work, these reference values support the proposed mechanism whereby the biopolymer shells contribute to corrosion protection by restricting oxygen transport toward the metal/electrolyte interface and thereby limiting cathodic oxygen reduction reactions.

3. 2. 3 EIS Investigation

Figure 9, **Figure 10**, and **Table 2** respectively showcase the Nyquist and Bode plots, employed one/two-time constant electrical circuits accompanied with the Electrochemical Impedance Spectroscopy (EIS) fittings details of dipped steel panels in the Blank and extract solutions of ZnP, ZnP@Ch and ZnP@Cel for distinct immersion times. The corrosion inhibition performance of ZnP, ZnP@Cel, and ZnP@Ch nanocomposites on mild steel in a 3.5 wt.% NaCl solution was rigorously evaluated using EIS. The Nyquist and Bode plots, alongside the fitted parameters detailed in **Table 3**, provide a quantitative and qualitative assessment of the protective films formed at the steel/electrolyte interface over a 24 h immersion period [30].

The electrochemical behavior was modeled using equivalent electrical circuits featuring one or two time constants, where R_s represents the solution resistance, R_{ct} is the charge-transfer resistance, and R_f denotes the resistance of a surface film [44,54]. The non-ideal capacitive behavior of the double layer and any surface films is represented by constant phase elements

(CPE_{dl} and CPE_f, respectively), whose admittance values (Y_0) and exponents (n) were used to calculate the effective capacitance (C_{dl} and C_f) using the **Equation (3**) and **(4)** [31]:

$$C_{dl} = (CPE_{dl} \times \left(\frac{R_s \times R_{ct}}{R_s + R_{ct}}\right)^{1-n})^{\frac{1}{n}} \quad \textbf{(3)}$$

$$C_f = (CPE_f^{\frac{1}{n}} \times R_f^{\frac{n-1}{n}}) \quad \textbf{(4)}$$

The exponent n serves as a critical indicator of interfacial homogeneity, with values closer to 1.0 signifying a more ideal capacitor and a smoother, more uniform surface [31,55]. The chi-square (χ^2) values reported in all electrochemical outcomes, ranging from 3.00×10^{-4} to 1.17×10^{-3}, confirm the excellent goodness of fit for all equivalent circuit models. The unprotected Blank sample exhibited consistently poor corrosion resistance. After 1 h, it showed a low R_{ct} of 1412 Ω·cm² and a high C_{dl} of 77.56 μF·cm⁻², indicative of a readily permeable interface. The data for 1 h and 5 h were fitted with a single and double time-constant model, respectively, suggesting the absence and in the present of a defined corrosion products film. By 24 h, a second time constant emerged, revealing a very porous rust film (R_f = 4.94 Ω·cm²) [1,15]. However, this native film was ineffective, as the overall impedance remained low (R_{ct} = 2005 Ω·cm²) and the double-layer capacitance, though calculated lower due to the new model, still reflected easy electrolyte access to the metal surface. The declining n_{dl} values (from 0.79 to 0.68) further confirm the increasing heterogeneity and defectiveness of the corroding surface [55]. The introduction of pristine ZnP led to a moderate improvement, necessitating a two-time-constant model from the outset. This confirms the formation of a zinc phosphate protective surface film [30,31]. The film resistance R_f was significant (1025-992.60 Ω·cm²), and the R_{ct} rechaed to 992.60 Ω·cm² after 24 h, surpassing the blank. However, the performance was unstable. The effective C_{dl} fluctuated considerably (227 to 405 to 142 μF·cm⁻²), and the film capacitance C_f remained very high (91.5-101.31 μF·cm⁻²), signaling that the deposited

ZnP layer is porous, hydrated, and unstable, offering only a partial physical barrier against chloride ion penetration [42,53].

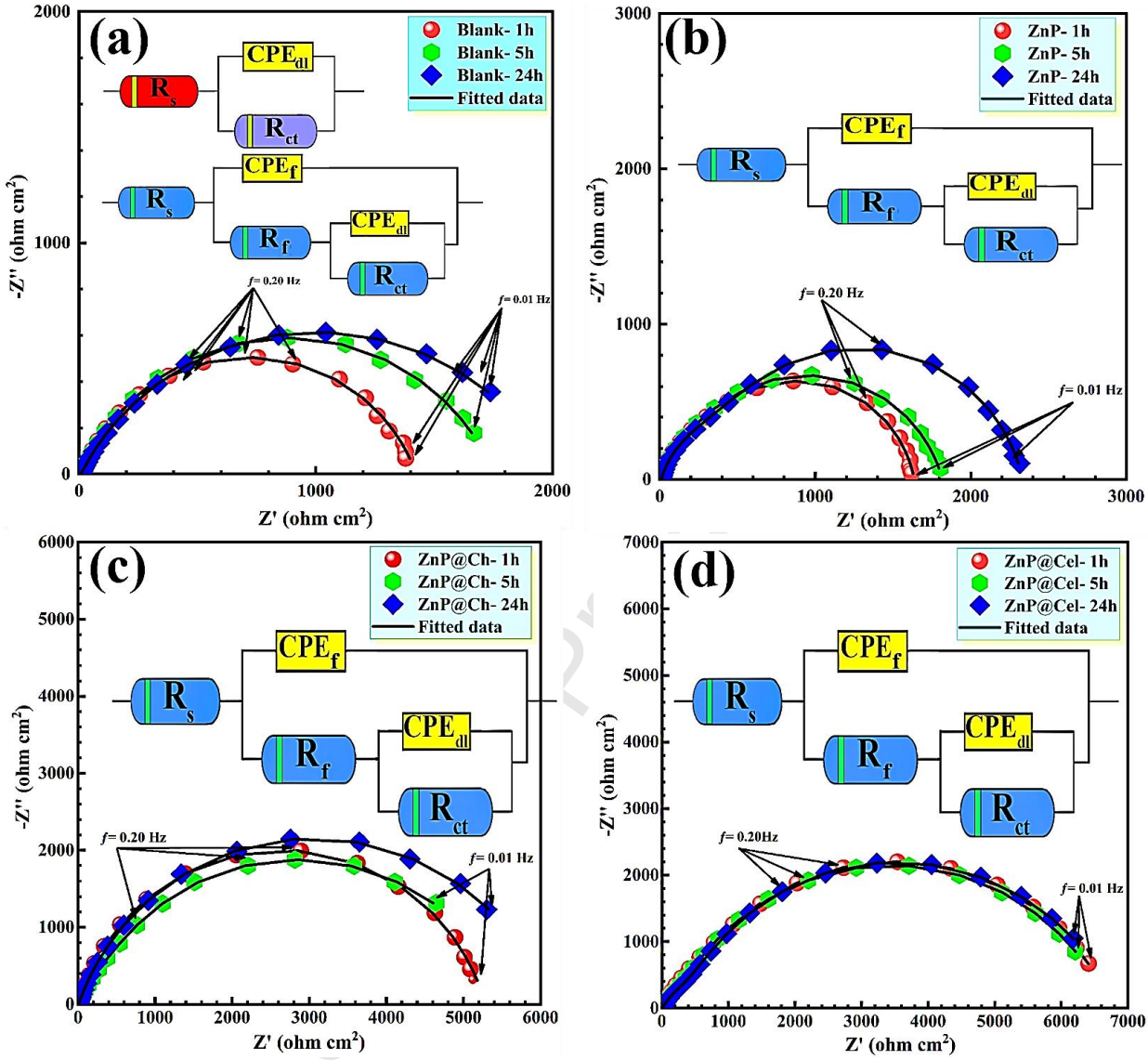

Figure 9. Nyquist diagrams with corresponding equivalent circuit models (single- and double-constant phase elements) employed for fitting the electrochemical impedance response of mild steel samples immersed for 1, 5, and 24 h in (a) Blank, (b) ZnP, (c) ZnP@Ch, and (d) ZnP@Cel media.

The ZnP@Ch nanocomposite provided the superior and consistent protection in comparison to ZnP samples. It exhibited excellent performance from the first hour immersion, with a high R_{ct}

of 4170 Ω·cm² and a low C_{dl} of 14.50 μF·cm⁻². Unlike other Blank and ZnP samples, its performance stabilized impressively over time, maintaining a very high R_{ct} of 5644 Ω·cm² and achieving the lower C_{dl} of 26.90 μF·cm⁻² at 24 h[14]. This superior performance in comparison to Blank and ZnP samples is attributed to the chitosan biopolymer, whose amino and hydroxyl groups possess strong chelating and adhesive properties [42,53]. These functionalities enable chitosan to adsorb tenaciously onto the steel surface, organizing a highly uniform and adherent mixed organic-inorganic interphase [2,9,13]. This interphase acts as a synergistic barrier, simultaneously reinforcing the zinc phosphate deposit and blocking both anodic and cathodic reaction sites. The steady n_{dl} values around 0.7-0.8 further attest to the formation of a homogenous and non-porous surface layer [55].

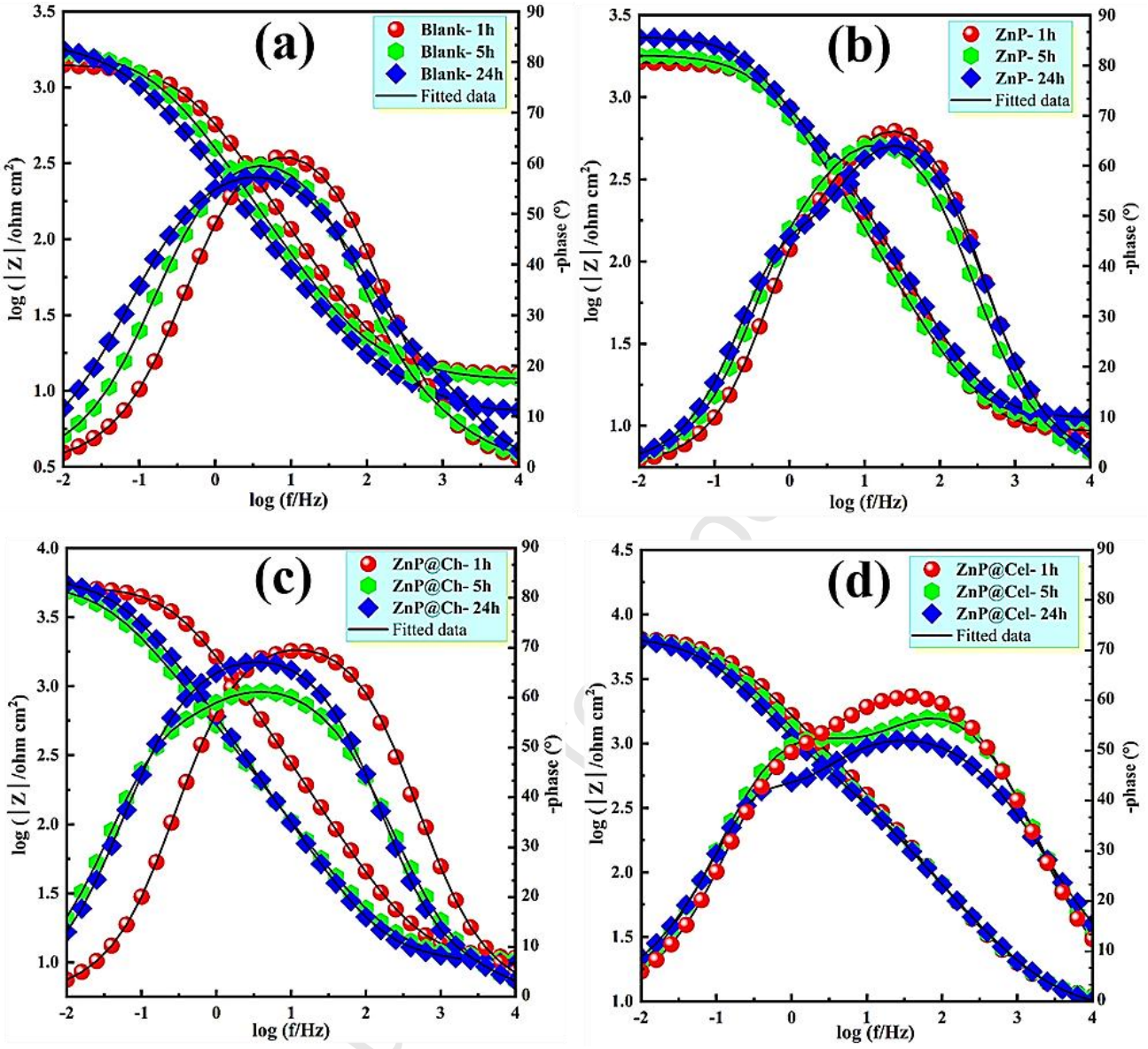

Figure 10. Bode and Phase Angle curves of fitting the electrochemical impedance response of mild steel panels diped for 1, 5, and 24 h in (a) Blank, (b) ZnP, (c) ZnP@Ch, and (d) ZnP@Cel media.

The ZnP@Cel nanocomposite demonstrated a significantly enhanced and more robust protective mechanism. At 1 h, the data fit a double time-constant model with a high R_{ct} of 4980 $\Omega \cdot cm^2$ and a suppressed C_{dl} of 1.33 $\mu F \cdot cm^{-2}$, suggesting rapid surface coverage. By 5 h, a effective dual-layer structure had formed, evidenced by a moderate R_{ct} of 1699 $\Omega \cdot cm^2$ and a drastically low C_{dl} of 386 $\mu F \cdot cm^{-2}$. This indicates that the cellulose shell acts as a stabilizing

hydrophilic matrix, facilitating the formation of a dense, cohesive organic-inorganic film that severely restricts electrolyte uptake and ion mobility [46,51].

Moreover, the R_{ct} increase slightly to 6127 $\Omega \cdot cm^2$ after 24 h, it remained the highest of all samples, and the C_{dl} was further reduced to 53.10 $\mu F \cdot cm^{-2}$, proving exceptional long-term barrier integrity. Comparable increases in charge-transfer resistance and reductions in corrosion current density have been reported for epoxy coatings reinforced with rGO/metal nitride nanocomposites[79].The very low calculated C_f of 28.59 $\mu F \cdot cm^{-2}$ at 24 h is a strong indicator of a highly impermeable film [16,24].

In fact, the EIS analysis unequivocally demonstrates that encapsulating zinc phosphate in biopolymers transforms its inhibition mechanism from one of unstable precipitation to one of intelligent surface modification. ZnP@Ch forms a rapidly established, dense physical barrier, while ZnP@Cel creates a highly adherent and stable electroactive barrier through chemisorption [29,31,53].

Both nanocomposites far outperform the bare steel and pristine ZnP, with ZnP@Cel showing the most consistent and efficient protection over the 24 h period, as directly evidenced by the sustained high charge-transfer resistance and minimal capacitive response across the entire frequency spectrum.

Table 3. The EIS fitting parameters obtained for mild steel specimens immersed in Blank electrolyte, ZnP, ZnP@Ch, and ZnP@Cel solutions at immersion intervals of 1, 5, and 24 h.

Sample	R_s[a]	CPE_f		R_f[d]	CPE_{dl}		R_{ct}[g]	C_{dl}[h]	C_f[i]
		Y_{0f}[b]	n_f[c]		Y_{0dl}[e]	n_{dl}[f]			
	$\Omega.cm^2$	$\mu\Omega^{-1} cm^{-2} s^n$	-	$\Omega.cm^2$	$\mu\Omega^{-1} cm^{-2} s^n$	-	$\Omega.cm^2$	$\mu F.cm^{-2}$	$\mu F.cm^{-2}$
Blank– 1h	12.73	-	-	-	332.40	0.79	1412	77.56	-
Blank– 5h	11.77	437.30	0.74	16.88	134.10	0.80	1725	28.59	80.12
Blank– 24h	7.41	46.7	0.97	4.94	858.20	0.68	2005	86.75	36.72
ZnP– 1h	9.25	140	0.85	1025	227	1	603.9	227	101.31
ZnP – 5h	10.53	211.30	0.81	1393	404.70	1	416	405	160.22
ZnP – 24h	11.05	136.30	0.83	992.60	252.60	0.91	1331	142	91.95
ZnP@Ch– 1h	9.64	107.10	0.74	2587	90.37	0.79	4170	14.50	68.76
ZnP@Ch– 5h	9.45	106.10	0.73	830.70	100.40	0.73	5901	8.03	45.09
ZnP@Ch – 24h	8.35	141.80	0.69	1231	125.90	0.81	5644	26.90	66.77
ZnP@Cel– 1h	10.49	116.50	0.82	296.10	1.326	1	4980	1.33	56.92
ZnP@Cel – 5h	10.07	464.20	0.73	3957	386.10	1	1699	386	576.55
ZnP@Cel – 24h	9.59	53.53	0.93	2.69	328.20	0.75	6127	53.10	28.59

[a] The standard deviation fluttered between 2.4% to 4.1%.

[b] The standard deviation fluttered between 3.1% to 5.1%.

[c] The standard deviation fluttered between 6.4% to 7.6%.

[d] The standard deviation fluttered between 5.4% to 8.7%.

[e] The standard deviation fluttered between 2.8% to 6.2%.

[f] The standard deviation fluttered between 5.4% to 6.6%.

[g] The standard deviation fluttered between 7.4% to 7.9%.

[h] The standard deviation fluttered between 11.7% to 14.3%.

[i] The standard deviation fluttered between 14.4% to 15.1%.

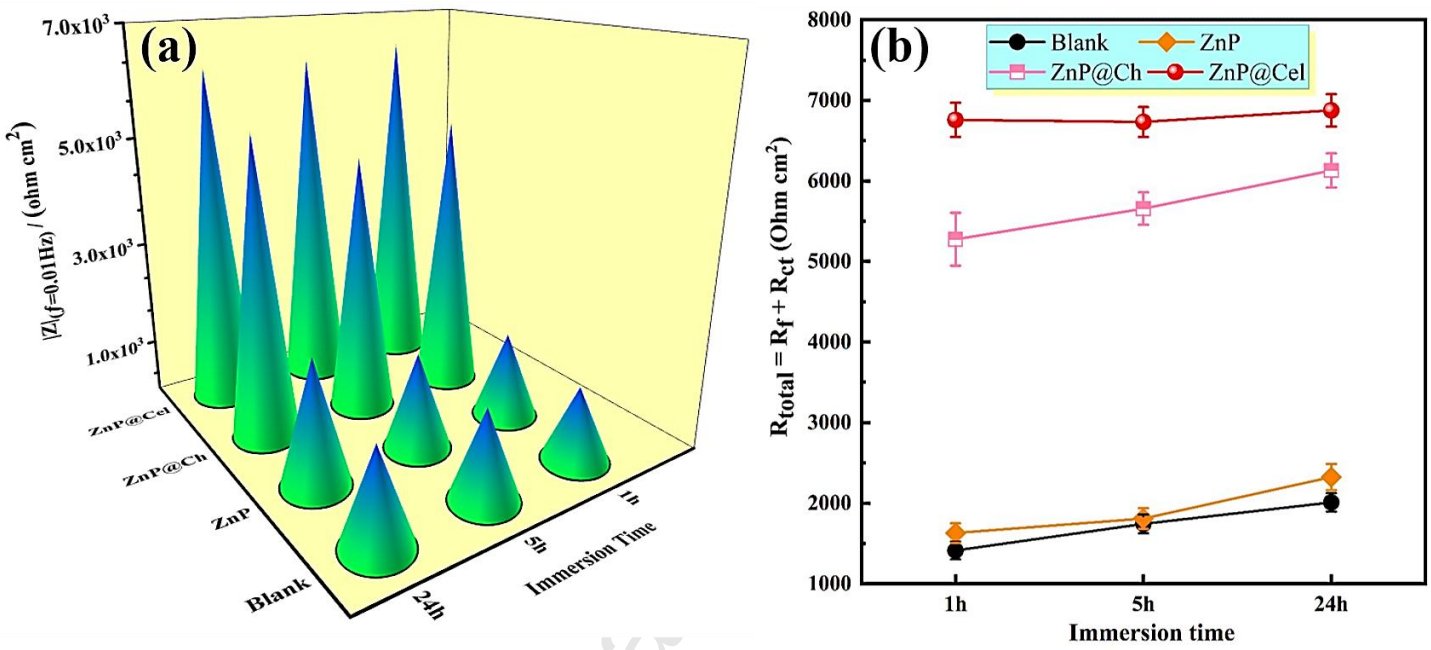

Figure 11. The (a) $|Z|_{0.01Hz}$ and (b) $R_{total}=R_{ct}+R_f$ for mild steel specimens exposed to 3.5 wt.% NaCl electrolyte (Blank), comparing with protected by ZnP, ZnP@Ch, and ZnP@Cel nanocomposite.

Figure 11 (a, b) illustrates the total resistance ($R_{total}=R_{ct}+R_f$) and the impedance modulus at 0.01 Hz ($|Z|_{0.01Hz}$) for mild steel specimens exposed to 3.5 wt.% NaCl electrolyte, comparing uncoated (blank) samples with those protected by ZnP, ZnP@Ch, and ZnP@Cel nanocomposite. The protective efficacy of the nanocomposites was further quantified by analyzing the low-frequency impedance modulus ($|Z|_{0.01Hz}$) and the sum of the charge-transfer and film resistances ($R_{total}=R_{ct}+R_f$), as these parameters are critical indicators of a coating's overall barrier performance against corrosion [7,8,13].

The $|Z|_{0.01Hz}$ value, representing the impedance at a very low frequency (0.01 Hz), is a robust measure of the system's DC-like resistance and directly correlates with the corrosion resistance, with higher values signifying more effective protection. The data for the Blank (unprotected) sample confirms its inherent susceptibility to corrosion. It exhibited the lowest initial $|Z|_{0.01Hz}$ value of 1399.2 Ω·cm² and R_{total} of 1412 Ω·cm² after 1 h immersion.

Although these values showed a slight increase over 24 h (reaching 1763.6 Ω·cm² and 2009.9 Ω·cm², respectively), this minor improvement is not indicative of effective protection. Instead, it is characteristic of the formation of a porous, non-protective rust layer whose slight thickening offers only a marginal increase in resistance while remaining highly permeable to water, oxygen, and chloride ions. The consistently low values underscore the absence of a true barrier film [9].

Incorporation of pristine ZnP led to a measurable but modest and unstable improvement in barrier properties. The $|Z|_{0.01Hz}$ and R_{total} values were consistently higher than those of the Blank sample at all immersion times (e.g., $|Z|_{0.01Hz}$ of 2309 Ω·cm² vs. 1764 Ω·cm² at 24 h). The upward trend over time (from 1630 to 2309 Ω·cm² for $|Z|_{0.01Hz}$) suggests the ongoing precipitation and growth of a zinc phosphate film on the steel surface [24]. However, the relatively low magnitude of these values, especially when compared to the biopolymer-modified samples, reveals the film's inherent limitations. It is likely a discontinuous, micro-cracked, or porous layer that provides incomplete coverage and an unstable barrier, which is prone to breakdown under prolonged exposure [60].

The nanocomposites ZnP@Cel and ZnP@Ch demonstrated a transformative enhancement in corrosion protection, outperforming both the Blank and pure ZnP by an order of magnitude. The $|Z|_{0.01Hz}$ and R_{total} values for these samples were exceptionally high from the initial immersion period and remained stable or even increased over time. The ZnP@Cel (zinc-

phosphate-cellulose) composite displayed outstanding performance, achieving the highest recorded values. Its $|Z|_{0.01Hz}$ was remarkably stable at approximately 6270-6441 Ω·cm² throughout the entire 24 h test, and its R_{total} increased from 6757 to 6875 Ω·cm². This exceptional stability indicates the rapid formation of an immensely dense and highly effective barrier layer [9,13,31].

The hydrophilic cellulose matrix acts as a stabilizer, facilitating the formation of a cohesive, low-porosity organic-inorganic composite film that drastically reduces electrolyte uptake and ion diffusion rates, resulting in a consistently high impedance response [24,31].

The ZnP@Ch composite also provided superior protection, characterized by a strong and steadily increasing impedance. Its $|Z|_{0.01Hz}$ and R_{total} values rose significantly from 5189 to 5473 Ω·cm² and from 5276 to 6130 Ω·cm², respectively, between 1 and 24 h. This progressive improvement points to an active protection mechanism.

The chitosan shell, rich in amino and hydroxyl groups, undergoes strong chemisorption onto the steel substrate, creating a uniform and adherent initial layer [24,30]. Over time, the continued interaction and possible reorganization of this chitosan-phosphate interphase leads to a further sealing of the surface, enhancing the barrier properties and maximizing the charge-transfer resistance [28,49].

Ultimately, the analysis of $|Z|_{0.01Hz}$ and R_{total} provides unequivocal evidence of the performance hierarchy: ZnP@Cel > ZnP@Ch >> ZnP > Blank. The biopolymer nanocomposites do not merely deposit a passive layer; they form a dynamic, resilient, and highly impermeable barrier at the metal-electrolyte interface. ZnP@Cel achieves this through the instant formation of a supremely dense physical shield, while ZnP@Ch accomplishes it through strong adsorption and the ongoing development of a reinforced mixed matrix [2,3,31].

Both mechanisms are vastly more effective than the simple precipitation of unmodified zinc phosphate or the formation of native rust, conclusively demonstrating the synergistic effect of combining inorganic inhibitors with organic biopolymer matrices for advanced corrosion protection.

3. 3 Antribaterial Behavior Investigation of Nanocomposites

The comprehensive evaluation of the antibacterial properties of zinc phosphate (ZnP), zinc-phosphate-chitosan (ZnP@Ch), and zinc-phosphate-cellulose (ZnP@Cel) nanocomposites, conducted through a multi-faceted experimental approach encompassing agar disk diffusion, colony-forming unit (CFU) counting, and MTT cytocompatibility assays, reveals a pronounced and mechanistically distinct enhancement in biocidal efficacy for the biopolymer-encapsulated composites. The antibacterial activity evaluation outcomes of the synthesized ZnP, ZnP@Ch, and ZnP@Cel nanocomposites were revealed in **Figure 12**, **Table 3** and **Table 4**, respectively. **Table 4** compared the antibacterial activity of ZnP, ZnP@Ch, and ZnP@Cel nanocomposites in the present work. Result has been shown that ZnP@Ch, and ZnP@Cel nanocomposites have good antibacterial power in comparison to ZnP nanocomposites.

Table 4. The inhibition Zone of ZnP, ZnP@Ch, and ZnP@Cel nanocomposites.

sample	Strain	Zone of inhibition (mm)
ZnP	Streptococcus faecalis	12
ZnP@Ch	S.mutans ATCC35668	18
ZnP@Cel	S.mutans ATCC35668	18

The agar diffusion test (**Figure 12** and **Table 5**), which qualitatively assesses the ability of leached antibacterial agents to diffuse through an agar medium and inhibit microbial growth, established a clear hierarchy of performance [61,62]. While pristine ZnP nanoparticles

exhibited a moderate inhibition zone of 12 mm against the Gram-positive bacterium Staphylococcus aureus, the ZnP@Ch and ZnP@Cel nanocomposites generated significantly larger zones of inhibition, measuring 18 mm each, not only against S. aureus but also against the Gram-negative Escherichia coli [63,64].

Table 5. Result of CFU test with Antibacterial Reduction for ZnP, ZnP@Ch, and ZnP@Cel nanocomposites.

Sample	Bacteria	Bacteria concentration CFU/ml	Number of colony CFU/ml	Log10 (number of colony)	Log10 CFU/ml reduction	Antibacterial Reduction (%)
Control	Streptococcus mutans	10^5	0.5×10^{19}	18.69	0	-
ZnP			1.39×10^{10}	10.14	5.49	99.9997%
ZnP@Ch			1.49×10^{10}	10.17	8.52	99.9999997%
ZnP@Cel			0	-	18.69	100 %

This immediate and broad-spectrum bactericidal effect, indicated by the larger clear zones, suggests that the biopolymer shells are not inert carriers but actively contribute to the antimicrobial mechanism, likely by facilitating a more uniform dispersion and sustained release of zinc ions (Zn^{2+}) from the phosphate core, thereby increasing the effective surface area and contact with bacterial cells [24].

In addition to reporting the absolute CFU counts, antibacterial reduction percentages were calculated to quantitatively evaluate bacterial inactivation by the developed nanocomposites. The antibacterial reduction efficiency (R) was determined using **Equation (5)** [24,87,88]:

$$R\ (\%)\ =\ \frac{CFU_{control} - CFU_{sample}}{CFU_{control}} \times\ 100 \qquad \textbf{(5)}$$

where CFUcontrol corresponds to the bacterial population in the untreated control group and CFUsample denotes the bacterial population after exposure to the respective nanocomposite. The resulting reduction percentages provide a more rigorous measure of antibacterial effectiveness than CFU values alone and confirm the superior bactericidal performance of ZnP@Cel and ZnP@Ch relative to pristine ZnP.

The quantitative CFU assay, which provides a highly accurate measure of bactericidal activity by counting viable cells after direct exposure to the nanomaterials, delivered even more compelling evidence of a powerful synergistic effect. After 48 h of exposure to a standardized suspension of Streptococcus mutans (1×10^5 CFU/mL), the treatments resulted in staggering logarithmic reductions in viable bacterial counts. Pristine ZnP achieved a significant 5.49 log10 reduction, equivalent to a 99.9997% elimination of the bacterial population [29,61]. To provide a more quantitative evaluation of antibacterial performance, the colony-forming unit (CFU) data were converted into antibacterial reduction percentages according to **Equation (5)**. The calculated reduction efficiencies were 99.9997% for ZnP, 99.9999997% for ZnP@Ch, and approximately 100% for ZnP@Cel, confirming the remarkable bactericidal activity of the biopolymer-modified nanocomposites [88,89]. These results demonstrate a clear performance hierarchy of ZnP@Cel > ZnP@Ch > ZnP and further highlight the synergistic effect of cellulose and chitosan shells in enhancing the antibacterial efficacy of zinc phosphate nanoparticles.

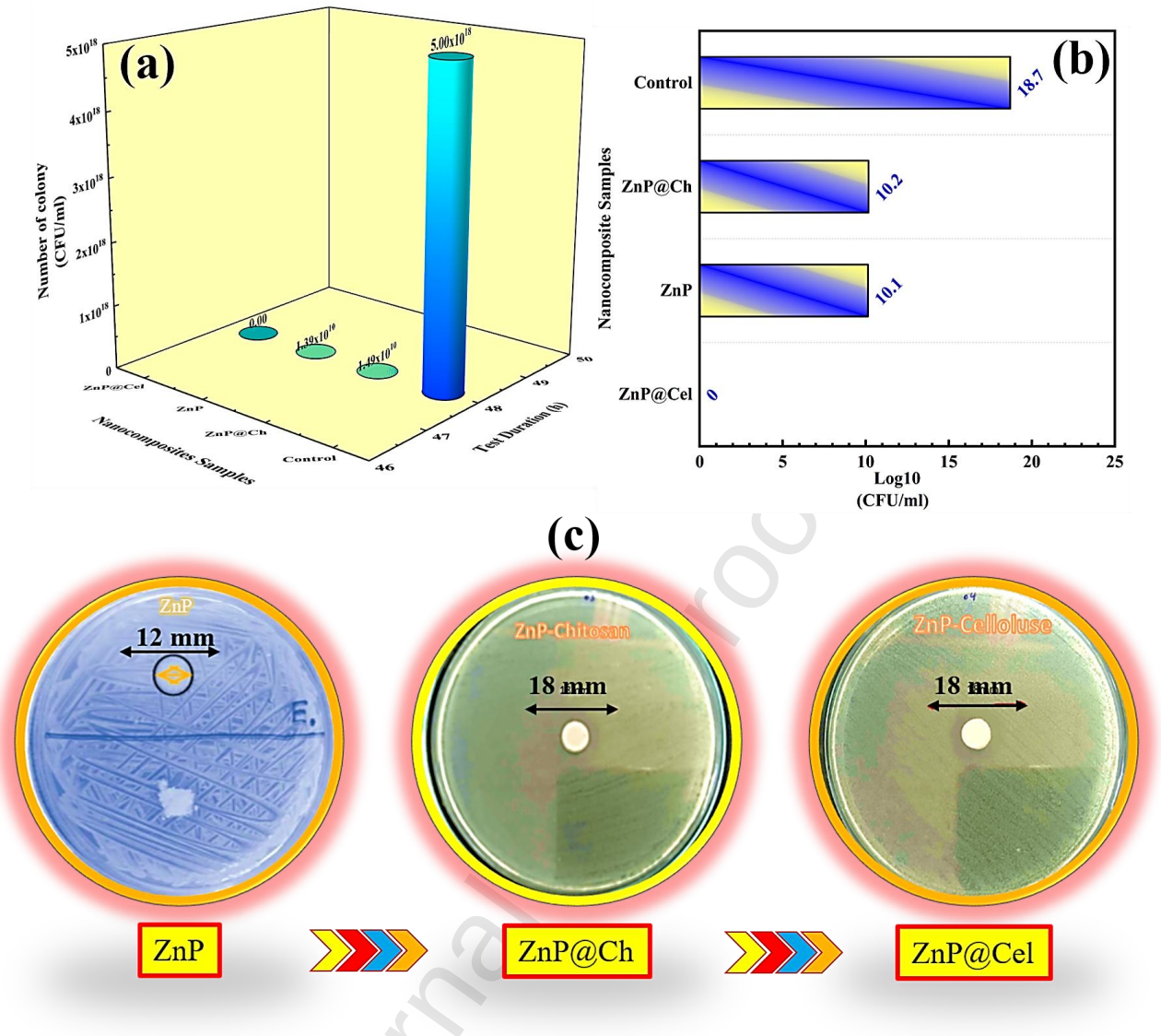

Figure 12. Antibacterial evaluation of the synthesized nanocomposites: (a) colony counts of Streptococcus mutans following 48 h incubation with ZnP, ZnP@Ch, and ZnP@Cel nanocomposites; (b) logarithmic (Log10) representation of colony-forming units; and (c) inhibition zone assay against the Gram-positive bacterium Staphylococcus aureus for comparative assessment of antibacterial efficacy. Data are presented as mean ± SD (n = 3). Statistical significance was evaluated using one-way ANOVA with $p < 0.05$ considered significant.

However, the biopolymer-modified composites far surpassed this performance. ZnP@Ch achieved an 8.52 log10 reduction, while ZnP@Cel demonstrated complete sterilization,

showing a total 18.69 log10 reduction with zero detectable colonies. This extraordinary efficacy can be attributed to the distinct functionalities of each biopolymer matrix [61].

For ZnP@Ch, the potent antimicrobial action is multifactorial: the protonated amino groups ($-NH_3^+$) of chitosan under physiological conditions electrostatically interact with and disrupt the negatively charged phospholipid membranes of bacteria, increasing permeability and facilitating the entry of lethal Zn^{2+} ions; simultaneously, the chitosan shell acts as a chelating agent, sequestering essential nutrients and metals from the bacterial environment, thereby inducing metabolic arrest [62].

While chitosan possesses inherent antibacterial activity due to its protonated amino groups, which electrostatically interact with negatively charged bacterial membranes, the superior overall antibacterial performance of ZnP@Cel (complete sterilization, 18.69 log10 reduction) compared to ZnP@Ch (8.52 log10 reduction) can be attributed to several factors. First, the cellulose shell provides superior dispersion and stabilization, effectively preventing agglomeration of ZnP nanoparticles and ensuring a maximized and uniform interface for bacterial contact, leading to more efficient Zn^{2+} release[90]. Second, the thicker cellulose shell (5.25 nm) compared to the chitosan shell (4 nm) provides better encapsulation and controlled release kinetics, allowing for sustained ion release over the 48 h incubation period. Third, the lower water content of cellulose (15% w/w) compared to chitosan (40% w/w) results in a more stable matrix that resists excessive swelling and maintains structural integrity, preventing rapid ion depletion. Fourth, the superior oxygen barrier properties of cellulose (Table 2) may reduce oxidative degradation of the nanocomposite and preserve its antibacterial activity[91]. Fifth, the stronger hydrogen-bonding network in cellulose, as evidenced by FTIR analysis, creates a more cohesive and stable shell that protects the ZnP core while allowing controlled ion diffusion. In contrast, while chitosan provides additional membrane-disrupting activity through its cationic nature, this effect may be counterbalanced by its higher water content and greater

swelling, which can lead to faster ion release and depletion, resulting in lower overall antibacterial efficacy over the extended 48 h period. Thus, the superior performance of ZnP@Cel arises from a synergistic combination of optimal nanoparticle dispersion, sustained ion release, and superior matrix stability.

For ZnP@Cel, the cellulose matrix, while less inherently bactericidal than chitosan, plays a critical role as a superior dispersant and stabilizer. It effectively prevents the agglomeration of ZnP nanoparticles, which is a common limitation that reduces reactive surface area, ensuring a maximized and uniform interface for bacterial contact and a more efficient release of antibacterial Zn^{2+} ions [62,64]. The antibacterial action of Zn^{2+} ions involves multiple pathways, including disruption of enzymatic functions (e.g., dehydrogenase inhibition), interference with membrane potential, and induction of oxidative stress through glutathione depletion, ultimately leading to bacterial cell death[90].

Furthermore, Zn^{2+} ions can catalyze the generation of reactive oxygen species (ROS) through Fenton-like reactions, resulting in lipid peroxidation, protein carbonylation, and DNA fragmentation, which collectively contribute to the bactericidal effect[92].

Membrane disruption occurs through two complementary pathways: (i) direct physical interaction between ZnP nanoparticles and bacterial cell walls, leading to structural damage and cytoplasmic leakage, and (ii) lipid peroxidation initiated by ROS and metal ions, which compromises membrane integrity[92].

Furthermore, the cytocompatibility assessment via MTT assay on L929 fibroblast cells is crucial, as it confirms that the dramatically enhanced antibacterial potency of these nanocomposites is not accompanied by increased cytotoxicity towards mammalian cells at concentrations up to 200 μg/mL. This indicates a favorable selective toxicity, a vital characteristic for any potential biomedical or hygienic application. In conclusion, the data

unequivocally demonstrates that the encapsulation of zinc phosphate within chitosan or cellulose matrices transforms it from a moderately effective antibacterial agent into a potent, broad-spectrum, and highly efficacious nanocomposite [6,61]. The synergy arises from the combined effects of the biopolymers membrane disruption and chelation for chitosan, and superior dispersion and stabilization for cellulose working in concert with the ion-release mechanism of the zinc phosphate core to achieve a powerful and comprehensive antibacterial action [18,19,63]. Moreover, the strong antibacterial activity of ZnP@Cel indicates its potential to inhibit biofilm formation on metallic surfaces, thereby preventing microbially induced corrosion (MIC). This additional functionality further reinforces the long-term stability of the protective coating in real-world applications.

The strong antibacterial activity of ZnP@Cel also indicates its potential to inhibit biofilm formation on metallic surfaces through several mechanisms: (i) prevention of initial bacterial adhesion due to the hydrophilic nature of the biopolymer shells, (ii) continuous release of Zn^{2+} ions that kill bacteria before they can establish a mature biofilm, and (iii) potential interference with quorum-sensing pathways. This additional functionality further reinforces the long-term stability of the protective coating in real-world applications by mitigating microbially induced corrosion (MIC).

4. Conclusion

This study demonstrates the successful design of eco-friendly zinc phosphate–biopolymer nanocomposites (ZnP@Cel and ZnP@Ch) that deliver efficient and sustainable corrosion and antibacterial protection for mild steel. The ZnP@Cel coating, in particular, exhibits superior barrier integrity and charge-transfer resistance due to its dense cellulose shell, which promotes strong adhesion and minimizes chloride and oxygen penetration. The ZnP@Ch composite also provides effective protection through coordination bonding between its amino/hydroxyl groups

and the steel surface. Both systems act as dual-functional, intelligent coatings capable of preventing electrochemical corrosion and microbial colonization. While the present characterization (XRD, FTIR, TEM, FESEM-EDS) confirms the core–shell morphology and homogeneous integration of the ZnP cores within the biopolymer shells, we acknowledge that advanced spectroscopic techniques such as XPS and Raman spectroscopy, as well as high-resolution elemental mapping, would provide additional confirmation of the chemical states and interfacial bonding. These analyses are planned for future work to further elucidate the structure property relationships. The present study was performed only in neutral saline media (3.5 wt.% NaCl, pH 6.5–7.2). Future work will systematically evaluate performance at acidic (pH 3–5) and alkaline (pH 9–11) conditions to assess the true environmental adaptability of the ZnP@Cel and ZnP@Ch nanocomposites. Overall, the ZnP@Cel nanocomposite emerges as a robust, eco-friendly, and scalable candidate for replacing conventional chromate-based coatings in marine, biomedical, and industrial applications. Future studies will focus on quantitative biofilm inhibition assays, evaluation against additional Gram-positive, Gram-negative, and MIC-associated bacterial strains, investigation of quorum-sensing interference mechanisms, and long-term biological safety assessment to further establish the multifunctional performance of ZnP-based biopolymer nanocomposites under realistic service conditions. Although the developed ZnP@Ch and ZnP@Cel nanocomposites exhibited promising corrosion inhibition and antibacterial performance under laboratory conditions, their long-term behavior in real marine and industrial environments remains to be validated. Therefore, the present results should be considered as an initial demonstration of their potential applicability. Future work will focus on long-term marine exposure studies, biofilm resistance and microbiologically influenced corrosion (MIC) assessments, as well as optimization of coating composition and thickness to further enhance protective performance under practical service conditions.

References

[1] H. Liang, X. Shi, Y. Li, Technologies in marine antifouling and anti-corrosion coatings: a comprehensive review, Coatings. 14 (2024) 1487.

[2] S. Asaldoust, B. Ramezanzadeh, Synthesis and characterization of a high-quality nanocontainer based on benzimidazole-zinc phosphate (ZP-BIM) tailored graphene oxides; a facile approach to fabricating a smart self-healing anti-corrosion system., J. Colloid Interface Sci. 564 (2020) 230–244. https://doi.org/10.1016/j.jcis.2019.12.122.

[3] S. Almathami, J. Venezuela, N. Yang, Y. Wang, Z. Mardina, M. Dargusch, Exploring the Influence of Biologically Relevant Ions on the Corrosion Behavior of Biodegradable Zinc in Physiological Fluids., ACS Biomater. Sci. Eng. 9 (2023) 2301–2316. https://doi.org/10.1021/acsbiomaterials.2c00901.

[4] S.S. Malheiros, M.H.R. Borges, E.C. Rangel, C.A. Fortulan, N.C. da Cruz, V.A.R. Barao, B.E. Nagay, Zinc-Doped Antibacterial Coating as a Single Approach to Unlock Multifunctional and Highly Resistant Titanium Implant Surfaces., ACS Appl. Mater. Interfaces. 17 (2025) 18022–18045. https://doi.org/10.1021/acsami.4c21875.

[5] K. Zuo, L. Wang, Z. Wang, Y. Yin, C. Du, B. Liu, L. Sun, X. Li, G. Xiao, Y. Lu, Zinc-Doping Induces Evolution of Biocompatible Strontium-Calcium-Phosphate Conversion Coating on Titanium to Improve Antibacterial Property., ACS Appl. Mater. Interfaces. 14 (2022) 7690–7705. https://doi.org/10.1021/acsami.1c23631.

[6] A. Priyadharshini, J.R. Xavier, Innovative reduced graphene oxide/polycysteine/coper titanate composite coating for corrosion-resistant and antibacterial tinplate in food packaging, Results Eng. 27 (2025) 106859. https://doi.org/https://doi.org/10.1016/j.rineng.2025.106859.

[7] R. Priyadharshini, J.R. Xavier, Recent Advances in Graphene-Based Nanocomposite

Coatings for Corrosion Resistance in the Automotive Industry and Their Smart Functional Applications, J. Bio- Tribo-Corrosion. 11 (2025) 113. https://doi.org/10.1007/s40735-025-01040-6.

[8] P. A., N. M., V. SP, J.R. Xavier, Development and performance evaluation of reduced graphene oxide/nitrides reinforced epoxy coatings for marine steel structures, Case Stud. Constr. Mater. 24 (2026) e05757. https://doi.org/https://doi.org/10.1016/j.cscm.2026.e05757.

[9] B. Liu, J. Sun, J. Zhao, X. Yun, Hybrid graphene and carbon nanotube–reinforced composites: polymer, metal, and ceramic matrices, Adv. Compos. Hybrid Mater. 8 (2024) 1. https://doi.org/10.1007/s42114-024-01074-3.

[10] J.R. Xavier, Novel multifunctional epoxy based graphitic carbon nitride/silanized TiO2 nanocomposite as protective coatings for steel surface against corrosion and flame in the shipping industry, J. Cent. South Univ. 31 (2024) 3394–3422. https://doi.org/10.1007/s11771-024-5788-z.

[11] C. Yang, S. Cui, R.K.Y. Fu, L. Sheng, M. Wen, D. Xu, Y. Zhao, Y. Zheng, P.K. Chu, Z. Wu, Optimization of the in vitro biodegradability, cytocompatibility, and wear resistance of the AZ31B alloy by micro-arc oxidation coatings doped with zinc phosphate, J. Mater. Sci. Technol. 179 (2024) 224–239. https://doi.org/https://doi.org/10.1016/j.jmst.2023.09.019.

[12] P. A, J.R. Xavier, Recent innovations in graphene-based nanocomposite coatings for enhanced flame retardancy in industrial applications, Polym. Degrad. Stab. 240 (2025) 111479. https://doi.org/https://doi.org/10.1016/j.polymdegradstab.2025.111479.

[13] J.R. Xavier, S.P. Vinodhini, B. Ramesh, Optimizing aluminum alloy performance for marine superstructures: Advanced nanocomposite coating for enhanced corrosion

resistance, flame retardancy, and mechanical strength, Polym. Degrad. Stab. 227 (2024) 110847. https://doi.org/https://doi.org/10.1016/j.polymdegradstab.2024.110847.

[14] D. Yan, Z. Zhang, W. Zhang, Y. Wang, M. Zhang, T. Zhang, J. Wang, Smart self-healing coating based on the highly dispersed silica/carbon nanotube nanomaterial for corrosion protection of steel, Prog. Org. Coatings. 164 (2022) 106694. https://doi.org/10.1016/j.porgcoat.2021.106694.

[15] J. Chavhan, M. Prabhakar, A. Ganapathi, M. Rohwerder, L. Neelakantan, Multifunctional Epoxy/PVDF smart coatings using ZIF-8 nanosensor for corrosion protection of mild steel: A study on synthesis and performance, Prog. Org. Coatings. 203 (2025) 109198. https://doi.org/10.1016/j.porgcoat.2025.109198.

[16] Q. Li, Y. Mi, W. Tan, Z. Guo, Highly efficient free radical-scavenging property of phenolic-functionalized chitosan derivatives: Chemical modification and activity assessment., Int. J. Biol. Macromol. 164 (2020) 4279–4288. https://doi.org/10.1016/j.ijbiomac.2020.08.250.

[17] Q. Li, X. Sun, G. Gu, Z. Guo, Novel Water Soluble Chitosan Derivatives with 1,2,3-Triazolium and Their Free Radical-Scavenging Activity., Mar. Drugs. 16 (2018). https://doi.org/10.3390/md16040107.

[18] N. Oladzadabbasabadi, A. Mohammadi Nafchi, F. Ariffin, M.M.J.O. Wijekoon, A.A. Al-Hassan, M.A. Dheyab, M. Ghasemlou, Recent advances in extraction, modification, and application of chitosan in packaging industry., Carbohydr. Polym. 277 (2022) 118876. https://doi.org/10.1016/j.carbpol.2021.118876.

[19] S. Tanpichai, A. Boonmahitthisud, N. Soykeabkaew, L. Ongthip, Review of the recent developments in all-cellulose nanocomposites: Properties and applications., Carbohydr. Polym. 286 (2022) 119192. https://doi.org/10.1016/j.carbpol.2022.119192.

[20] A. Mohammadkhani, F. Mohammadkhani, N. Farhadyar, M.S. Sadjadi, E. Kianfar, Novel nanocomposite zinc phosphate/ polyvinyl alcohol / carboxymethyl cellulose: Synthesis, characterization and investigation of antibacterial and anticorrosive properties, Case Stud. Chem. Environ. Eng. 9 (2024) 100591. https://doi.org/10.1016/j.cscee.2023.100591.

[21] N.R. Mohammed, M. Mneimne, R.G. Hill, M. Al-Jawad, R.J.M. Lynch, P. Anderson, Physical chemical effects of zinc on in vitro enamel demineralization, J. Dent. 42 (2014) 1096–1104. https://doi.org/10.1016/j.jdent.2014.04.014.

[22] J.R. Xavier, Multifunctional nanocomposite coatings for superior anticorrosive, flame retardant and mechanical properties in aerospace components, Surfaces and Interfaces. 38 (2023) 102832. https://doi.org/https://doi.org/10.1016/j.surfin.2023.102832.

[23] S.P. Vinodhini, J. Christina X, P. Kumaresan, G. Anitha, J.R. Xavier, Recent developments in MXene-Based nanocomposites for superior corrosion protection and supercapacitor performance, J. Power Sources. 661 (2026) 238651. https://doi.org/https://doi.org/10.1016/j.jpowsour.2025.238651.

[24] Y. Liu, C. Chen, T. Liang, Y. Wang, R. Zhao, G. Li, C. Bai, Y. Wu, F. Yu, L. Sheng, R. Zhang, Y. Zhao, In vitro long-term antibacterial performance and mechanism of Zn-doped micro-arc oxidation coatings, Colloids Surfaces B Biointerfaces. 233 (2024) 113634. https://doi.org/https://doi.org/10.1016/j.colsurfb.2023.113634.

[25] H. Cai, X. Li, Y. Zhang, C. Yang, S. Cui, L. Sheng, D. Xu, R.K.Y. Fu, X. Tian, P.K. Chu, Z. Wu, A high corrosion-resistant waterborne epoxy resin coating improved by addition of multi-interface structured zinc phosphate particles, J. Mater. Res. Technol. 26 (2023) 7829–7844. https://doi.org/https://doi.org/10.1016/j.jmrt.2023.09.109.

[26] Y. Cui, X. Zhao, Z. Jin, X. Ji, J. Duan, B. Hou, Construction of smart coatings containing

core-shell nanofibers with self-healing and self-reporting properties, Prog. Org. Coatings. 204 (2025) 109240. https://doi.org/10.1016/j.porgcoat.2025.109240.

[27] N. Afrose, R. Chakraborty, K. Rajendran, Plasma-polymerized chitosan/agarose/chitosan-agarose composite coatings for antibacterial and antibiofilm wound dressings: A review., Int. J. Biol. Macromol. 320 (2025) 145873. https://doi.org/10.1016/j.ijbiomac.2025.145873.

[28] Y. Jia, H. Zhang, A Hydrophilic Lubricating Coating with Dual Functions of Antibacterial Adhesion and Urease-Responsive Bactericidal Activity for Urinary Tract Implantable Devices., ACS Appl. Mater. Interfaces. 17 (2025) 33730–33744. https://doi.org/10.1021/acsami.5c07616.

[29] S. Peng, Y. Liu, W. Zhao, X. Liu, R. Yu, Y. Yu, Construction of pH-responsive hydrogel coatings on titanium surfaces for antibacterial and osteogenic properties., Front. Chem. 13 (2025) 1546637. https://doi.org/10.3389/fchem.2025.1546637.

[30] J.K. Singh, S. Mandal, H.-S. Lee, H.-M. Yang, Effect of Chloride Ions Concentrations to Breakdown the Passive Film on Rebar Surface Exposed to L-Arginine Containing Pore Solution., Mater. (Basel, Switzerland). 14 (2021). https://doi.org/10.3390/ma14195693.

[31] P. Vashishth, H. Bairagi, R. Sehrawat, B. Mangla, Environmentally Sustainable Approach of Corrosion Inhibition of Mild Steel in 1 N HCl and 1 N H 2 SO 4 via Antihistamine Loratadine (LT) and Its Amine Derivatives: Computational and Experimental Analysis, ACS Omega. 10 (2025) 5332–5350. https://doi.org/10.1021/acsomega.4c06238.

[32] A. Mohammadkhani, S.M. Seyed, N. Farhadyar, F. Mohammadkhani, Facile Preparation and Characterization of Alginate and Triton X-100 Zinc Phosphate modified

Surface Nanocrystals as a Novel Anti-corrosive and Antibacterial agent, Res. J. Biotechnol. 18 (2023) 91–101. https://doi.org/10.25303/1812rjbt910101.

[33] A. Mohammadkhani, F. Mohammadkhani, M.S. Sadjadi, N. Farhadyar, M.J. Soltanian Fard, E. Kianfar, M. Zakani, Preparation and characterization of anticorrosive and antibacterial coatable nanocomposite based on zinc phosphate modified by Hydroxy Apatite/alginate: Investigation of electrochemical impedance spectroscopy (EIS), Case Stud. Chem. Environ. Eng. 9 (2024) 100694. https://doi.org/10.1016/j.cscee.2024.100694.

[34] R.Y. Aguirre-Loredo, A.I. Rodríguez-Hernández, E. Morales-Sánchez, C.A. Gómez-Aldapa, G. Velazquez, Effect of equilibrium moisture content on barrier, mechanical and thermal properties of chitosan films, Food Chem. 196 (2016) 560–566.

[35] M. Garg, V. Apostolopoulou-Kalkavoura, M. Linares, T. Kaldéus, E. Malmström, L. Bergström, I. Zozoulenko, Moisture uptake in nanocellulose: the effects of relative humidity, temperature and degree of crystallinity, Cellulose. 28 (2021) 9007–9021.

[36] M. Akbari, R. Naderi, B. Ramezanzadeh, Tailoring exfoliated 2D Mo-PDA nanopetals as sustainable intelligent anti-corrosion nanoreservoir for upgrading the self-healing/barrier function of epoxy coatings, Chem. Eng. J. 490 (2024) 151494. https://doi.org/10.1016/j.cej.2024.151494.

[37] F.C. Yazdic, A. Karaman, G. Torgut, N.K. Ayhan, Antibacterial activity of novel synthesized chitosan-graft-poly(N-tertiary butylacrylamide)/neodymium composites for biomedical application., J. Basic Microbiol. 63 (2023) 1049–1056. https://doi.org/10.1002/jobm.202300004.

[38] M. Ramezani Farani, P. Khadive Parsi, G. Riazi, M. Shafiee Ardestani, H. Saligeh Rad, Extending the application of a magnetic PEG three-part drug release device on a

graphene substrate for the removal of Gram-positive and Gram-negative bacteria and cancerous and pathologic cells., Drug Des. Devel. Ther. 13 (2019) 1581–1591. https://doi.org/10.2147/DDDT.S181090.

[39] D. Karolina, M.-S. Maja, D.-S. Magdalena, Z. Grazyna, Identification of treated Baltic amber by FTIR and FT-Raman - A feasibility study., Spectrochim. Acta. A. Mol. Biomol. Spectrosc. 279 (2022) 121404. https://doi.org/10.1016/j.saa.2022.121404.

[40] S. Mitra, K. Werling, E.J. Berquist, D.S. Lambrecht, S. Garrett-Roe, CH Mode Mixing Determines the Band Shape of the Carboxylate Symmetric Stretch in Apo-EDTA, Ca(2+)-EDTA, and Mg(2+)-EDTA., J. Phys. Chem. A. 125 (2021) 4867–4881. https://doi.org/10.1021/acs.jpca.1c03061.

[41] A. Pal, S.C. Pal, K. Otsubo, D.-W. Lim, S. Chand, H. Kitagawa, M.C. Das, A Phosphate-Based Silver-Bipyridine 1D Coordination Polymer with Crystallized Phosphoric Acid as Superprotonic Conductor., Chemistry. 26 (2020) 4607–4612. https://doi.org/10.1002/chem.201905650.

[42] S. Aisawa, N. Horiguchi, C. Chida, J. Sang, H. Hirahara, A. Yamagishi, H. Sato, Nanoscale chirality generated in zinc(II) orthophosphate clusters: evidence by vibrational circular dichroism., Nanoscale. 16 (2024) 20589–20595. https://doi.org/10.1039/d4nr03809f.

[43] L.-L. Dang, Z.-B. Sun, W.-L. Shan, Y.-J. Lin, Z.-H. Li, G.-X. Jin, Coordination-driven self-assembly of a molecular figure-eight knot and other topologically complex architectures., Nat. Commun. 10 (2019) 2057. https://doi.org/10.1038/s41467-019-10075-6.

[44] Y. Cozzens, P. Wang, J.E. Whitten, Adsorption of l-Cysteine and Cysteamine on Zinc Oxide Nanoparticles., Langmuir. 40 (2024) 23538–23548.

https://doi.org/10.1021/acs.langmuir.4c03497.

[45] G.D. Kumar, M. Banasiewicz, D. Jacquemin, D.T. Gryko, Switch-On Diketopyrrolopyrrole-Based Chemosensors for Cations Possessing Lewis Acid Character., Chem. Asian J. 16 (2021) 355–362. https://doi.org/10.1002/asia.202001376.

[46] Y. Hattori, H. Mori, J. Chou, M. Otsuka, Mechanochemical synthesis of zinc-apatitic calcium phosphate and the controlled zinc release for bone tissue engineering., Drug Dev. Ind. Pharm. 42 (2016) 595–601. https://doi.org/10.3109/03639045.2015.1061537.

[47] K. Kodama, A. Valanezhad, M. Khodaei, S. Safaee, S. Jafarnia, M. Nesabi, S. Abe, I. Watanabe, H. Murata, A novel coating layer on zirconia using modified zinc phosphatizing method., Dent. Mater. J. 40 (2021) 870–876. https://doi.org/10.4012/dmj.2020-253.

[48] M. Otsuka, H. Saito, T. Sasaki, Analytical Evaluation of Wet and Dry Mechanochemical Syntheses of Calcium-Deficient Hydroxyapatite Containing Zinc Using X-ray Diffractometry and Near-Infrared Spectroscopy., Pharmaceutics. 14 (2022). https://doi.org/10.3390/pharmaceutics14102105.

[49] S.P. Vinodhini, J.R. Xavier, Recent progress in graphene-based nanocomposites for enhanced energy storage and corrosion protection, J. Mater. Sci. 60 (2025) 14837–14879. https://doi.org/10.1007/s10853-025-11307-5.

[50] M. Gouda, M.M. Khalaf, K. Shalabi, M.A. Al-Omair, H.M.A. El-Lateef, Synthesis and Characterization of Zn-Organic Frameworks Containing Chitosan as a Low-Cost Inhibitor for Sulfuric-Acid-Induced Steel Corrosion: Practical and Computational Exploration., Polymers (Basel). 14 (2022). https://doi.org/10.3390/polym14020228.

[51] H. Elham, S. Roya, H. Adalat, P. Hanieh, Investigating Biological Properties of Zinc

Oxide/Curcumin Nanocomposites Synthesized from Stachys byzantina Extract by Green Synthesis., Comb. Chem. High Throughput Screen. 26 (2023) 517–526. https://doi.org/10.2174/1386207325666220408093646.

[52] T. Miri, D. Seifzadeh, Z. Rajabalizadeh, Smart epoxy coating containing inhibitor-loaded cellulose nanocrystals for corrosion protection of steel, Surf. Coatings Technol. 477 (2024) 130241.

[53] S. Sridevi, S. Sutha, L. Kavitha, D. Gopi, Physicochemical and biological behaviour of biogenic derived hydroxyapatite and carboxymethyl cellulose/sodium alginate biocomposite coating on Ti6Al4V alloy for biomedical applications, Mater. Chem. Phys. 254 (2020) 123455. https://doi.org/10.1016/j.matchemphys.2020.123455.

[54] D.S. Chauhan, M.A.J. Mazumder, M.A. Quraishi, K.R. Ansari, Chitosan-cinnamaldehyde Schiff base: A bioinspired macromolecule as corrosion inhibitor for oil and gas industry, Int. J. Biol. Macromol. 158 (2020) 127–138. https://doi.org/10.1016/j.ijbiomac.2020.04.200.

[55] R.A. Farghali, A.M. Fekry, R.A. Ahmed, H.K.A. Elhakim, Corrosion resistance of Ti modified by chitosan–gold nanoparticles for orthopedic implantation, Int. J. Biol. Macromol. 79 (2015) 787–799. https://doi.org/10.1016/j.ijbiomac.2015.04.078.

[56] S. Zarayneh, A.A. Sepahi, M. Jonoobi, H. Rasouli, Comparative antibacterial effects of cellulose nanofiber, chitosan nanofiber, chitosan/cellulose combination and chitosan alone against bacterial contamination of Iranian banknotes., Int. J. Biol. Macromol. 118 (2018) 1045–1054. https://doi.org/10.1016/j.ijbiomac.2018.06.160.

[57] Q. Zhu, S. Liu, J. Sun, J. Liu, C.J. Kirubaharan, H. Chen, W. Xu, Q. Wang, Stimuli-responsive cellulose nanomaterials for smart applications, Carbohydr. Polym. 235 (2020) 115933. https://doi.org/10.1016/j.carbpol.2020.115933.

[58] Y. Su, K. Wang, J. Gao, Y. Yang, Y.-X. Qin, Y. Zheng, D. Zhu, Enhanced cytocompatibility and antibacterial property of zinc phosphate coating on biodegradable zinc materials, Acta Biomater. 98 (2019) 174–185.

[59] S. Chen, Y. Li, S. Ren, Y. Yang, Z. Hou, S. Han, W. Zhang, J. Guo, J. Hu, X. Zhang, Amorphous zinc phosphate nanoclusters loaded polycarbonate thermosensitive hydrogel: An innovative strategy for promoting wound healing, Mater. Today Bio. 29 (2024) 101266.

[60] R. Salazar, V. Salas-Gomez, A.A. Alvarado, H. Baykara, Preparation, Characterization and Evaluation of Antibacterial Properties of Polylactide-Polyethylene Glycol-Chitosan Active Composite Films., Polymers (Basel). 14 (2022). https://doi.org/10.3390/polym14112266.

[61] M.A. Baltazar-Zamora, D. M Bastidas, G. Santiago-Hurtado, J.M. Mendoza-Rangel, C. Gaona-Tiburcio, J.M. Bastidas, F. Almeraya-Calderon, Effect of Silica Fume and Fly Ash Admixtures on the Corrosion Behavior of AISI 304 Embedded in Concrete Exposed in 3.5% NaCl Solution., Mater. (Basel, Switzerland). 12 (2019). https://doi.org/10.3390/ma12234007.

[62] S. Yin, H. Yang, Y. Dong, C. Qu, J. Liu, T. Guo, K. Duan, Environmentally favorable magnesium phosphate anti-corrosive coating on carbon steel and protective mechanisms., Sci. Rep. 11 (2021) 197. https://doi.org/10.1038/s41598-020-79613-3.

[63] A.R. Khan, H.-J. Zhang, Z. Jun, Z. Maosheng, S.M. Eldin, I. Siddique, Electrochemical corrosion protection of neat and zinc phosphate modified epoxy coating: A comparative physical aging study on Al alloy 6101., Front. Chem. 11 (2023) 1142050. https://doi.org/10.3389/fchem.2023.1142050.

[64] A. Habibiyan, B. Ramezanzadeh, M. Mahdavian, M. Kasaeian, Facile size and

chemistry-controlled synthesis of mussel-inspired bio-polymers based on Polydopamine Nanospheres: Application as eco-friendly corrosion inhibitors for mild steel against aqueous acidic solution, J. Mol. Liq. 298 (2020) 111974. https://doi.org/10.1016/j.molliq.2019.111974.

[65] M. Mahdavian, R. Naderi, Corrosion inhibition of mild steel in sodium chloride solution by some zinc complexes, Corros. Sci. 53 (2011) 1194–1200. https://doi.org/10.1016/j.corsci.2010.12.013.

[66] V. A.D, B. Panda, Corrosion behaviour of galvanised steel in alkaline sodium chloride solution, Adv. Mater. Process. Technol. 00 (2021) 1–15. https://doi.org/10.1080/2374068X.2021.1953916.

[67] A. Chaouiki, M. Chafiq, M. Rbaa, R. Salghi, B. Lakhrissi, I.H. Ali, S. Bashir, I.-M. Chung, Comprehensive assessment of corrosion inhibition mechanisms of novel benzimidazole compounds for mild steel in HCl: An experimental and theoretical investigation, J. Mol. Liq. 320 (2020) 114383. https://doi.org/10.1016/j.molliq.2020.114383.

[68] P. Kong, H. Feng, N. Chen, Y. Lu, S. Li, P. Wang, Polyaniline/chitosan as a corrosion inhibitor for mild steel in acidic medium, RSC Adv. 9 (2019) 9211–9217. https://doi.org/10.1039/C9RA00029A.

[69] M. Akbari, R. Naderi, B. Ramezanzadeh, Novel manufacturing of intelligent hierarchical molybdenum-polydopamine hollow nanocarriers for smart coating, Appl. Mater. Today. 33 (2023) 101880. https://doi.org/10.1016/j.apmt.2023.101880.

[70] A. Heidarian, M. Akbari, Polymeric Ionic Liquids as Novel Corrosion Inhibitors: Synthesis, Characterization, and Inhibition Mechanism, in: Polym. as Corros. Inhib., Royal Society of Chemistry, 2025: pp. 304–324.

https://doi.org/10.1039/9781837677214-00304.

[71] M.M. Solomon, S.A. Umoren, I.I. Udosoro, A.P. Udoh, Inhibitive and adsorption behaviour of carboxymethyl cellulose on mild steel corrosion in sulphuric acid solution, Corros. Sci. 52 (2010) 1317–1325. https://doi.org/10.1016/j.corsci.2009.11.041.

[72] A. Heidarian, M. Akbari, Corrosion Inhibition Mechanism of Polymers: Effect of Different Parameters and the Nature of the Metal/Electrolyte System, in: Polym. as Corros. Inhib., Royal Society of Chemistry, 2025: pp. 36–57. https://doi.org/10.1039/9781837677214-00036.

[73] M.G. Golafshani, H. Tavakoli, S.A. Hosseini, M. Akbari, MD and DFT computational simulations of Caffeoylquinic derivatives as a bio-corrosion inhibitor from quince extract with experimental investigation of corrosion protection on mild steel in 1M H2SO4, J. Mol. Struct. 1275 (2023) 134701. https://doi.org/10.1016/j.molstruc.2022.134701.

[74] B.L. Butler, P.J. Vergano, R.F. Testin, J.M. Bunn, J.L. Wiles, Mechanical and barrier properties of edible chitosan films as affected by composition and storage, J. Food Sci. 61 (1996) 953–956.

[75] M. Gällstedt, M.S. Hedenqvist, Oxygen and water barrier properties of coated whey protein and chitosan films, J. Polym. Environ. 10 (2002) 1–4.

[76] J. Bosch, U. Martin, W. Aperador, J.M. Bastidas, J. Ress, D.M. Bastidas, Corrosion Behavior of High-Mn Austenitic Fe–Mn–Al–Cr–C Steels in NaCl and NaOH Solutions, Materials (Basel). 14 (2021) 425. https://doi.org/10.3390/ma14020425.

[77] I.B. Obot, I.B. Onyeachu, A.M. Kumar, Sodium alginate: A promising biopolymer for corrosion protection of API X60 high strength carbon steel in saline medium,

Carbohydr. Polym. 178 (2017) 200–208. https://doi.org/10.1016/j.carbpol.2017.09.049.

[78] M.H. BinSabt, F.A. Azeez, N. Suleiman, Eco-friendly Silane-Based Coating for Mitigation of Carbon Steel Corrosion in Marine Environments., ACS Omega. 8 (2023) 12886–12898. https://doi.org/10.1021/acsomega.3c00013.

[79] J. N, T. K, J.R. Xavier, Advanced epoxy coatings with rGO/metal nitride nanocomposites for superior corrosion protection and mechanical durability in industrial applications, Results Eng. 27 (2025) 106464. https://doi.org/https://doi.org/10.1016/j.rineng.2025.106464.

[80] M. Nawaz, R.A. Shakoor, N. Al-Qahtani, J. Bhadra, N.J. Al-Thani, R. Kahraman, Polyolefin-Based Smart Self-Healing Composite Coatings Modified with Calcium Carbonate and Sodium Alginate, Polymers (Basel). 16 (2024) 636. https://doi.org/10.3390/polym16050636.

[81] Z. Chen, X. Li, B. Gong, N. Scharnagl, M.L. Zheludkevich, H. Ying, W. Yang, Double Stimuli-Responsive Conducting Polypyrrole Nanocapsules for Corrosion-Resistant Epoxy Coatings, ACS Appl. Mater. Interfaces. 15 (2023) 2067–2076. https://doi.org/10.1021/acsami.2c17466.

[82] R. Naderi, M. Mahdavian, M.M. Attar, Electrochemical behavior of organic and inorganic complexes of Zn(II) as corrosion inhibitors for mild steel: Solution phase study, Electrochim. Acta. 54 (2009) 6892–6895. https://doi.org/10.1016/j.electacta.2009.06.073.

[83] S. Mandal, J.K. Singh, D.-E. Lee, T. Park, Ammonium Phosphate as Inhibitor to Mitigate the Corrosion of Steel Rebar in Chloride Contaminated Concrete Pore Solution, Molecules. 25 (2020) 3785. https://doi.org/10.3390/molecules25173785.

[84] D. Jasenska, V. Kasparkova, K.A. Radaszkiewicz, Z. Capakova, J. Pachernik, M. Trchova, A. Minarik, J. Vajdak, T. Barta, J. Stejskal, M. Lehocky, T.H. Truong, R. Moucka, P. Humpolicek, Conducting composite films based on chitosan or sodium hyaluronate. Properties and cytocompatibility with human induced pluripotent stem cells., Carbohydr. Polym. 253 (2021) 117244. https://doi.org/10.1016/j.carbpol.2020.117244.

[85] A. Sanmugam, D. Shanthi, A.B. Sairam, R.S. Kumar, A.I. Almansour, N. Arumugam, A. Kavitha, H.-S. Kim, D. Vikraman, Fabrication of chitosan/fibrin-armored multifunctional silver nanocomposites to improve antibacterial and wound healing activities., Int. J. Biol. Macromol. 257 (2024) 128598. https://doi.org/10.1016/j.ijbiomac.2023.128598.

[86] N.G. Kandile, R.A. Elzamly, M.I. Mohamed, H.T. Zaky, D.R.K. Harding, H.M. Mohamed, New sustainable antimicrobial chitosan hydrogels based on sulfonamides and its nanocomposites: Fabrication and characterization., Int. J. Biol. Macromol. 239 (2023) 124280. https://doi.org/10.1016/j.ijbiomac.2023.124280.

[87] Q. Kong, H. Zhang, Y. Lan, X. Shi, Z. Fang, Q. Chang, J. Liu, C. Wei, Functional graphene oxide for organic pollutants removal from wastewater: a mini review., Environ. Technol. 44 (2023) 3183–3195. https://doi.org/10.1080/09593330.2022.2053754.

[88] L. Duan, F. Yan, L. Zhang, B. Liu, Y. Zhang, X. Tian, Z. Liu, X. Wang, S. Wang, J. Tian, H. Bao, T. Liu, ZnO@Polyvinyl Alcohol/Poly(lactic acid) Nanocomposite Films for the Extended Shelf Life of Pork by Efficient Antibacterial Adhesion., ACS Omega. 7 (2022) 44657–44669. https://doi.org/10.1021/acsomega.2c03016.

[89] E.N. Zare, P. Makvandi, B. Ashtari, F. Rossi, A. Motahari, G. Perale, Progress in

Conductive Polyaniline-Based Nanocomposites for Biomedical Applications: A Review., J. Med. Chem. 63 (2020) 1–22. https://doi.org/10.1021/acs.jmedchem.9b00803.

[90] T. Jan, S. Azmat, Q. Mansoor, H.M. Waqas, M. Adil, S.Z. Ilyas, I. Ahmad, M. Ismail, Superior antibacterial activity of ZnO-CuO nanocomposite synthesized by a chemical Co-precipitation approach., Microb. Pathog. 134 (2019) 103579. https://doi.org/10.1016/j.micpath.2019.103579.

[91] S. Wang, J. Xue, M. He, X. Wang, H. Qi, Mechanisms of Cu2+ Immobilization Using Carbonyl Iron Powder–Biochar Composites for Remediating Acidic Soils from Copper Sulfide Mining Areas, Sustainability. 17 (2025) 4281. https://doi.org/10.3390/su17104281.

[92] D. Wang, C. Yuan, Y. Li, S. Bai, J. Feng, Y. Wang, Y. Fang, Z. Zhang, Chelation of the Optimal Antifungal Pogostone Analogue with Copper(II) to Explore the Dual Antifungal and Antibacterial Agent., J. Agric. Food Chem. 72 (2024) 3894–3903. https://doi.org/10.1021/acs.jafc.3c07050.

[93] M. Malefioudaki, A. Misra, N. Sbeity, J. Zueco-Vincelle, M.A. Laguna-Bercero, A. Koerdt, R. Martín-Rapún, S.G. Mitchell, Multifunctional polyoxomolybdate ionic liquid coatings for mitigating microbiologically influenced corrosion, Mater. Horizons. 12 (2025) 4648–4661. https://doi.org/10.1039/D5MH00373C.

Ms. Faezeh Mohammadhani holds an M.Sc. in Environmental Engineering (Environmental Pollution) from Islamic Azad University, North Tehran Branch. She is currently a researcher at Nano Pouyesh Yekta Company, specializing in the synthesis and application of functional nanomaterials for environmental and industrial purposes. Her work includes developing inorganic nanoparticles and nanocomposites for pharmaceutical degradation, pollutant adsorption, and industrial wastewater treatment, as well as corrosion-resistant and antibacterial coatings for oil refineries, petrochemical plants, hospitals, and food packaging. She has co-authored several publications on nanotechnology, wastewater treatment, corrosion protection, and antimicrobial materials. Her research interests encompass environmental nanotechnology, advanced oxidation processes, nanostructured adsorbents, smart coatings, and sustainable nanomaterials.

Dr. Arezoo Mohammadhani received her Ph.D. in Inorganic Chemistry from the Islamic Azad University, Central Tehran Branch, Iran. She is an active researcher in inorganic nanomaterials, currently contributing to R&D at Nano Pouyesh Yekta and Nano Sabz Golbaharan Companies, where she focuses on corrosion-resistant nanocomposites, antibacterial nanomaterials, and multifunctional coatings for industrial, environmental, and biomedical applications. Her work spans protective coatings, dental materials, wound dressings, smart packaging, heterogeneous catalysts, and nanostructured adsorbents for pollutant removal and water purification. She has also contributed to the development of nanocarrier systems for targeted drug delivery, integrating inorganic chemistry with biomaterials and pharmaceutical sciences. Dr. Mohammadhani has authored numerous peer-

reviewed publications and book chapters in nanotechnology, environmental catalysis, and biomedical drug delivery. Her research interests include multifunctional nanocomposites, antimicrobial materials, environmental catalysis, water/air purification, and advanced drug delivery systems.

Dr. Nazanin Farhadyar earned her Ph.D. in Inorganic Chemistry and is a faculty member at the Islamic Azad University, Pishva–Varamin Branch, Iran, with over 20 years of academic experience in teaching, research, and graduate supervision. She also serves as CEO of Nano Pouyesh Yekta Company, leading research and industrial development in advanced nanomaterials for applications including pollutant adsorption, air purification, coatings, ceramics, smart packaging, tissue engineering, drug delivery, and catalysts. She holds more than 16 national patents and has authored over 50 peer-reviewed publications in inorganic chemistry, nanotechnology, and materials science. Dr. Farhadyar has supervised more than 59 M.Sc. and Ph.D. students as principal advisor, and has served for over ten years on the Editorial Board of the Journal of Archaeology and Archaeometry, Islamic Azad University, Pishva–Varamin Branch. Her research interests include nanostructured materials, functional nanocomposites, environmental remediation, catalytic systems, and biomedical nanotechnology.

Dr. Payam Hayati was born in Shiraz, Iran, in 1983 and is originally from **Vahdatiyeh, Bushehr Province, Iran**. He is a **UK Global Talent Visa** holder and worked as a Postdoctoral Researcher at the Department of Biotechnology and Life Sciences (DBSV), **University of Insubria**, Italy, where he investigated chiral copper–amino acid catalysts for the ring-opening polymerization of cyclic esters. He previously completed a postdoctoral fellowship at the **Iran University of Science and Technology (IUST)**, Tehran, on metal–organic frameworks (MOFs) for photocatalytic environmental remediation.

Dr. Hayati received his **Ph.D. in Inorganic Chemistry** from the **University of Sistan and Baluchestan**, Iran, and earned an **M.Sc. degree from the Universitat Autònoma de Barcelona (UAB), Spain**. He also conducted research at the **Catalan Institute of Nanoscience and Nanotechnology (ICN2-CSIC), Spain**, and the **University of Milan, Italy**, through international collaborations.

His research focuses on inorganic and coordination chemistry, MOFs, coordination polymers, crystal engineering, catalysis, and functional nanomaterials. He has authored **more than 60 peer-reviewed publications**, several book chapters, and holds a **patent for a mercury-based antibacterial and anticancer nanocomplex**. He serves as **Guest Editor, Topical Issue Editor, Editorial Board Member, and reviewer** for leading journals published by **ACS, Elsevier, Wiley, Springer Nature, RSC, MDPI, and Frontiers**, and maintains active international collaborations with researchers across **Europe, North America, Asia, and Africa**. His achievements include the **Best Presentation Award** at the **4th International Conference on Polymer Chemistry (Stockholm, Sweden)** and recognition as a **Top National Researcher** in Iran.

Dr. Constantinos D. Zeinalipour-Yazdi is currently an assistant professor in chemistry at Northeastern University London where he started as a lecturer in July 2023. He has an MA in chemistry from San Diego State University (2003) and a PhD in chemistry from the University of California, San Diego and SDSU (JDP) received in 2006. He then held postdoctoral positions at the University of Cyprus, Cardiff University, University of Warwick, University College London, Research Complex at Harwell (2006-2018). He also held lecturer positions in

physical, computational and materials chemistry at the University of Greenwich (2018-2020), University of East London (2020-2022), Middlesex University (2020-2021, 2023).

His research experience spans the area of investigating the reaction mechanism of important catalytic reactions using computational methods. He has made significant contribution in elucidating new mechanisms for the synthesis of ammonia and hydrazine on various metal nitrides and for the water-gas shift (WGS) over metal nanoparticles.

Dr. Saeid Khodabakhshi is an organic chemist with postdoctoral and fellowship experience in Iran, Spain, and the UK since earning his PhD in 2013. His research focuses on carbon-based materials for energy storage and gas capture. He has authored 107 publications and received a Marie Curie Fellowship. Currently, he develops pharmaceutical APIs.

Faezeh Mohammadkhani

Arezoo Mohammadkhani

Nazanin Farhadyar

Payam Hayati

Constantinos D. Zeinalipour-Yazdi

Saeed Khodabakhshi

Declaration of Interest

The authors declare that they have no known competing financial interests or personal relationships that could have appeared to influence the work reported in this paper. Furthermore, the authors confirm that no funding or external support has influenced the design, analysis, or interpretation of the results presented in this study.

Graphical abstract

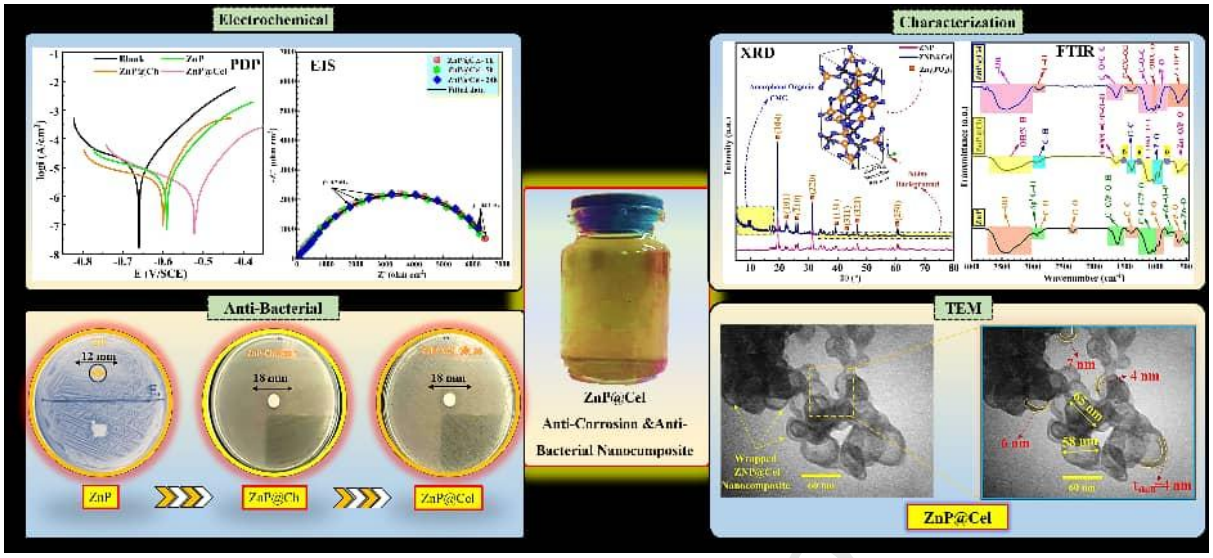

Research Highlights

- ZnP@Cel nanocomposite achieves 75.3% corrosion inhibition efficiency (i_{corr}= 1.76 µA/cm²) in 3.5 wt.% NaCl.
- High charge-transfer resistance of 6127 Ω·cm² confirms superior barrier formation.
- Complete bacterial eradication (100% kill rate, 18.69 log reduction) against *S. mutans*.
- Dual synergistic mechanism: physical barrier (biopolymer shell) and Zn^{2+}/PO_4^{3-} passivation.
- Core–shell architecture with 4–5 nm biopolymer shells on 36–62 nm ZnP nanoparticles.